Ringdown and tide: Fingerprints of dark matter halo profiles

Arkadip Bhowmik,[1,*] Avijit Chowdhury,[2,†] and Sayan Chakrabarti[1,‡]
[1]*Department of Physics, Indian Institute of Technology Guwahati, Assam-781039, India*
[2]*Indian Institute of Astrophysics, Block 2, 100 Feet Road, Koramangala, Bengaluru 560034, India*

(Received 20 August 2026; accepted 21 September 2026; published 22 October 2026)

Astrophysical black holes (BHs) are not isolated, but embedded in matter supplied by their host galaxies. We study how the shape of a surrounding dark matter halo modifies the ringdown and tidal response of an asymptotically flat, static, spherically symmetric BH. The halo is modeled as an anisotropic Einstein cluster with vanishing radial pressure and a generalized (α, β, γ) density profile, supplemented by an inner cutoff near the BH and, where required, an outer tidal truncation. We derive the axial gravitational perturbation equation and compute the quasinormal mode (QNM) spectrum using sixth-order Wentzel-Kramers-Brillouin (WKB) methods and time-domain evolutions. The halo redshifts both the oscillation frequency and the damping rate, by an amount set not only by the halo compactness but also by the profile parameters: the inner logarithmic slope γ dominates for centrally concentrated halos, while α and β give subleading but profile-dependent corrections. In the eikonal limit, the shift is governed by a single redshift integral encoding the halo mass distribution outside the light ring, explaining the close correspondence between the QNM frequencies, the light ring frequency, and the Lyapunov exponent. We also show that different combinations of compactness and profile shape can yield nearly degenerate ringdown spectra. Time-domain evolutions confirm the WKB frequencies and display the expected late-time Price-law decay, with an intermediate tail controlled by the outer density falloff for slowly decaying profiles. Finally, we compute the static axial tidal Love number and show that it probes the halo with a radial weighting different from the ringdown sector. The combined ringdown and tidal response therefore provides a possible way to distinguish environmental effects from genuine deviations of the vacuum BH geometry.

DOI: 10.1103/mvys-wjf4

I. INTRODUCTION

Since the landmark first detection of gravitational waves (GWs) in 2015 from the binary black hole (BBH) merger GW150914 by the LIGO Scientific Collaboration, GW astronomy has rapidly evolved from the discovery phase to an era of increasingly precise measurements [1,2]. The observations by the LIGO-Virgo-KAGRA (LVK) Collaboration have now reported a large and steadily growing population of compact binary coalescences, with BBH mergers forming the dominant class of sources [3–7]. The first three observing runs (O1–O3) yielded 90 confident detections. The subsequent Gravitational-Wave Transient Catalog releases (4.0 and 5.0), covering O4a and O4b, respectively, increased the total number of confirmed GW events to 390 [8]. This rapid increase in both the number and the quality of detections is changing the role of GW observations. They are no longer used only to establish the existence of BBH mergers; they are now becoming precision probes of black hole spacetimes and of the astrophysical environments in which these objects form and evolve.

A particularly clean part of the gravitational waveform is the ringdown phase, during which the remnant BH relaxes through damped oscillations known as quasinormal modes (QNMs) [9,10]. These modes are fixed by the background geometry together with purely ingoing boundary conditions at the horizon and purely outgoing conditions at infinity. In vacuum general relativity, the Kerr QNM spectrum depends only on the remnant mass and spin, making ringdown a direct probe of the strong-field regime and the basis of black hole (BH) spectroscopy and tests of the Kerr hypothesis [10–15].

Ground-based detectors primarily probe stellar-mass BHs, whose dominant ringdown frequencies lie in the range ~ 10–10^2 Hz [2], whereas the Laser Interferometer Space Antenna will target massive and supermassive BH mergers with masses $\sim 10^5$–$10^7 M_\odot$ or larger and ringdown frequencies in the millihertz band [16–20]. Their potentially high signal-to-noise ratios make them promising systems for precision ringdown studies. It is therefore important to identify effects that can shift the spectrum away from the vacuum Kerr or Schwarzschild prediction, including modified gravity, exotic compact objects, and

*Contact author: b.arkadip@iitg.ac.in
†Contact author: avijit.chowdhury@iiap.res.in
‡Contact author: sayan.chakrabarti@iitg.ac.in

 © 2026 American Physical Society

additional fields [2,21,22], as well as environmental corrections arising within general relativity because astrophysical BHs are not perfectly isolated [2,23].

Supermassive BHs are ubiquitous in galactic centers. Observations of stellar orbits around Sagittarius A* [24,25], together with very long baseline interferometric measurements of water megamasers [26], provide strong evidence for compact objects with masses in the range 10^6–$10^9 M_\odot$ [27]. Empirical relations such as the $M_{\rm BH}$–σ relation further indicate a close connection between central BHs and their host galaxies [27–29]. Since galaxies are embedded in extended dark matter (DM) halos [30–32], supermassive BHs should not be regarded as perfectly isolated vacuum objects; the surrounding matter distribution may leave measurable imprints on strong-field observables [22,23,33–39]. The DM distribution near a BH is shaped by several competing processes. BH growth can steepen the central density and produce a DM spike [40–42], whereas capture of low angular momentum particles depletes the density close to the horizon [41]. Stellar scattering, baryonic feedback, BH mergers, and long-term galactic evolution can further reshape the inner profile [42–45]. At larger radii, the halo contributes to the galactic potential and may influence the evolution of massive BH binaries. The surrounding matter is therefore not merely a passive background, but can affect both the premerger dynamics and the ringdown of the remnant [37,46]. The influence of matter environments on BH oscillations has received growing attention in recent years [47–49]. Even a dilute distribution can modify the background geometry, shift the light ring properties, and alter the effective potential governing perturbations, thereby introducing environmental corrections to the QNM spectrum. Recent studies of BHs surrounded by generic matter distributions and specific DM halos have shown that the corresponding QNM frequencies can be redshifted relative to the vacuum Schwarzschild values [50–53]. Although this redshift is strongly influenced by the mass and compactness of the surrounding matter, its dependence on the detailed shape of the halo is rarely talked about. In the generalized relativistic DM halo profile parametrized by three parameters (α, β, γ) [see Eq. (10)], the inner logarithmic slope γ, the outer logarithmic slope β, and the transition sharpness α can redistribute matter differently and may therefore leave distinct imprints on the strong-field geometry. This leads to the central question of the present work: at fixed halo compactness, does the ringdown depend only on the total surrounding mass, or can it also distinguish between different halo profiles?

In order to answer the question, we study axial gravitational perturbations of an asymptotically flat, static, spherically symmetric BH embedded in relativistic DM halos. The halo is modeled as an anisotropic fluid using the generalized Einstein-cluster construction [54,55], in which DM particles move on circular geodesics with random orientations. After averaging, the effective fluid has vanishing radial pressure and nonzero tangential pressure. For each density profile, the mass and redshift functions are obtained from the background field equations together with asymptotic flatness. In the axial sector, density and pressure perturbations do not enter the master equation directly [50,56]. The remaining matter perturbations are associated with the axial components of the fluid velocity and the auxiliary spatial vector. Of these, the velocity perturbation is fixed by requiring the perturbed flow to remain irrotational, whereas the perturbation of the auxiliary vector is chosen to be consistent with conservation of the perturbed energy-momentum tensor. The linearized equations reduce to a Regge-Wheeler-type equation whose effective potential depends on the halo mass function, redshift factor, and density profile. It recovers the Schwarzschild Regge-Wheeler equation when the halo is removed, while a nonzero DM distribution modifies the potential barrier and hence both the oscillation frequency and damping rate of the QNMs.

We compute the QNM spectrum in both the frequency and time domains. In the frequency domain, the WKB approximation [57–59] provides the fundamental modes and selected higher multipoles of the halo profile, while the Gundlach-Price-Pullin [60] characteristic scheme is used to extract the ringdown signal directly from time evolution. We also calculate the light ring frequency and its principal Lyapunov exponent [61] as a useful analytic guide, because in the eikonal limit, these quantities determine the oscillation frequency and damping rate, respectively, and therefore provide a simple interpretation of the halo-induced QNM shifts. Our results show that the axial QNM frequencies are redshifted relative to the Schwarzschild values. The shift increases with halo compactness, but it also depends on the shape parameters of the density profile. The inner logarithmic slope γ gives the strongest effect for centrally concentrated halos, while β and α produce subleading but nontrivial corrections. We find that different combinations of compactness and profile shape can lead to nearly identical QNM shifts, producing a degeneracy in the ringdown sector. Time-domain evolutions confirm the WKB frequencies and show the expected late-time Price-law decay, with an intermediate tail controlled by the outer density falloff for slowly decaying profiles.

We also compute the static axial tidal Love number (TLN), which characterizes the conservative response of a compact object to an external tidal field. In four-dimensional vacuum general relativity, the static polar and axial TLNs of a Schwarzschild BH vanish identically [62–74]. Nonzero TLNs can nevertheless arise when the assumptions of the vacuum Schwarzschild solution are relaxed, including in other spacetime dimensions, modified gravity, nonasymptotically flat geometries, altered near-horizon boundary conditions, or matter environments [56,64,75–97]. Focusing on the environmental contribution, we derive

the axial TLNs of the (α,β,γ) halos to leading order in compactness and confirm the analytic results through numerical solutions, in agreement with Ref. [95]. Interestingly enough, we find that the tidal response is complementary to the ringdown spectrum: QNM shifts are governed mainly by an inner-weighted redshift integral, whereas the axial TLN depends on a higher radial moment and is therefore more sensitive to the outer halo and its truncation radius. Thus, halo configurations that are nearly degenerate in ringdown can be distinguished through their tidal response. The physical implications of our results are threefold. First, matter-induced shifts should be taken into account in precision tests of BH spectroscopy before a deviation from the vacuum QNM spectrum is interpreted as evidence for new gravitational physics. Such a deviation may instead contain information about the environment surrounding the remnant. Second, ringdown observations may provide a new way to probe the distribution of DM in the strong-field region, which is difficult to access through conventional galactic measurements. Third, the degeneracy between halo compactness and profile shape in the ringdown spectrum can be reduced by combining QNM measurements with tidal Love numbers. The two observables probe different parts of the halo: the ringdown is more sensitive to the inner region, whereas the tidal response is weighted more strongly toward the outer halo. For ordinary stellar-mass BBH mergers, the surrounding DM environment is expected to be weak, so any constraints should be interpreted cautiously. Massive BH binaries and extreme-mass-ratio inspirals are more promising, since they may remain embedded in denser galactic environments and can be observed with high precision by future space-based detectors [16,23,98–100]. This paper is organized as follows. In Sec. II, we construct the static BH spacetime embedded in a DM halo and introduce the generalized (α,β,γ) density profiles considered in this work. In Sec. III, we derive the axial gravitational perturbation equations and obtain the corresponding Regge-Wheeler-type master equation. In Sec. IV, we present the frequency-domain analysis of the quasinormal modes, including the WKB calculation, the eikonal interpretation in terms of the light ring frequency and Lyapunov exponent, the dependence of the spectrum on the halo parameters, and its observational implications. In Sec. V, we perform time-domain evolutions to validate the frequency-domain results and analyze the late-time behavior of the perturbations. In Sec. VI, we investigate the static axial tidal Love numbers of BHs surrounded by DM halos and discuss their complementarity with the ringdown observables in Sec. VII. We conclude in Sec. VIII with a summary of our main results and their implications for environmental effects in GW observations. Additional analytic derivations and supplementary results on Secs. IV A and IV B are, respectively, presented in Appendixes A and B. Throughout this work, we use geometrized units with $G = c = 1$.

II. BACKGROUND GEOMETRY AND DENSITY PROFILES

This section reviews the construction of an asymptotically flat, static, and spherically symmetric BH spacetime embedded in a DM environment with generic density profiles [101].

A. Background geometry

We consider a static, spherically symmetric spacetime described by the line element

$$d\bar{s}^2 = -f(r)dt^2 + \frac{dr^2}{1-\frac{2m(r)}{r}} + r^2 d\Omega^2, \tag{1}$$

where $d\Omega^2$ denotes the metric on the unit two-sphere, $m(r)$ is the mass function, and $f(r)$ determines the redshift factor.

Following Refs. [51–53,56,94], we model the DM environment using the generalized Einstein-cluster formalism [54,55]. An Einstein cluster consists of collisionless particles moving on circular geodesics with all possible orientations. After averaging over orbital phases and directions, the effective stress-energy tensor takes the form

$$\langle T^{\mu\nu}\rangle = \frac{n}{m_p}\langle P^\mu P^\nu\rangle, \tag{2}$$

where n is the proper number density, m_p is the particle rest mass, and P^μ is the four-momentum satisfying the geodesic equation. This averaging ensures stationarity and spherical symmetry.

The resulting configuration is equivalent to an anisotropic fluid with vanishing radial pressure and nonzero tangential pressure. The spacetime, therefore, satisfies Einstein's equations,

$$\bar{G}_{\mu\nu} = 8\pi\bar{T}_{\mu\nu}, \tag{3}$$

with an effective stress-energy tensor

$$\bar{T}_{\mu\nu} = (\bar{\rho}+\bar{p}_t)\bar{u}_\mu\bar{u}_\nu + (\bar{p}_r-\bar{p}_t)\bar{w}_\mu\bar{w}_\nu + \bar{p}_t\bar{g}_{\mu\nu}, \tag{4}$$

where $\bar{u}^\mu$ is the normalized fluid four-velocity, such that $\bar{u}^\mu\bar{u}_\mu = -1$ and $\bar{w}^\mu$ is a unit spacelike vector orthogonal to $\bar{u}^\mu$, such that $\bar{w}_\mu\bar{w}^\mu = 1$ and $\bar{u}^\mu\bar{w}_\mu = 0$. The quantities $\bar{\rho}$, $\bar{p}_t$, and $\bar{p}_r = 0$ represent the energy density, transverse pressure, and (vanishing) radial pressure of the background DM fluid, respectively.

For a given density profile, the mass function is determined by the continuity equation,

$$m'(r) = 4\pi r^2\bar{\rho}(r). \tag{5}$$

The metric function $f(r)$ follows from the rr component of the Einstein equations,

$$\frac{f'(r)}{f(r)} = \frac{2m(r)/r}{r - 2m(r)}, \tag{6}$$

while the Bianchi identities determine the tangential pressure

$$\bar{p}_t(r) = \frac{m(r)}{2[r - 2m(r)]}\bar{\rho}(r). \tag{7}$$

Together, the functions $m(r)$ and $f(r)$ completely specify the spacetime geometry and its geodesic properties.

To construct the spacetime, we follow the numerical procedure of Ref. [52]. For a chosen DM density profile (see Sec. II B), Eq. (5) is first integrated outward from the horizon, $r_h = 2M_{\rm BH}$, yielding the mass function $m(r)$. The metric function $f(r)$ is then obtained by integrating Eq. (6) inward from r_∞ (numerically $\sim 10^{10} M_{\rm BH}$), imposing asymptotic flatness through the boundary conditions

$$m(r_\infty) = M_{\rm ADM} = M_{\rm BH} + M_{\rm halo}, \tag{8}$$

$$f(r_\infty) = 1 - \frac{2m(r_\infty)}{r_\infty}, \tag{9}$$

where $M_{\rm ADM}$ denotes the Arnowitt-Deser-Misner (ADM) mass and $M_{\rm halo}$ is the total mass of the DM halo.

B. Environmental density profiles

We consider a parametrized density profile [102,103], described by

$$\bar{\rho}(r) = \bar{\rho}_0 \left(\frac{r}{a_0}\right)^{-\gamma} \left[1 + \left(\frac{r}{a_0}\right)^{\alpha}\right]^{\frac{\gamma-\beta}{\alpha}}, \tag{10}$$

where $\bar{\rho}_0 = 2^{(\beta-\gamma)/\alpha}\bar{\rho}(a_0)$ is a scale factor and a_0 is a characteristic scale radius. The parameter γ controls the inner logarithmic slope of the profile, β determines the large radius falloff, and α fixes the sharpness of the transition between the inner and outer regimes with larger values of α producing a more abrupt transition [102,104].

For $r \gg a_0$, we note from Eq. (10) that

$$\bar{\rho} \approx \bar{\rho}_0 \left(\frac{r}{a_0}\right)^{-\beta}, \tag{11}$$

whereas for $r \ll a_0$,

$$\bar{\rho} \approx \bar{\rho}_0 \left(\frac{r}{a_0}\right)^{-\gamma}. \tag{12}$$

We require $\beta > \gamma \geq 0$ to ensure a monotonically decreasing density profile, where $\gamma = 0$ corresponds to a central core and $\gamma > 0$ to a central cusp. Profiles that suffer mass divergence at large distance are truncated at the tidal radius $r_t > a_0$ beyond which tidal stripping renders the spherically symmetric assumption unphysical.[1] For benchmarking, we also consider the Einasto density profile [105,106], which according to recent N-body cold dark matter simulations, provides an excellent fit to a wide range of DM halos. The Einasto profile is given by

$$\bar{\rho}(r) = \bar{\rho}_e \exp\left\{-d_n\left[(r/r_e)^{1/n} - 1\right]\right\}, \tag{13}$$

where r_e denotes the radius of the sphere containing half of the total mass, and $\bar{\rho}_e$ is the mass density at $r = r_e$ with $n = 6$ and $d_n = 53/3$ [107,108]. Throughout the work, we set $r_e = a_0$ for brevity.

The presence of a nonrotating BH sitting at the core of the DM distribution is expected to redistribute the DM resulting in an overdensity with a sharp cutoff close to the horizon at $r = 4M_{\rm BH}$. The radius $r = 4M_{\rm BH}$ corresponds to the radius of the unstable circular orbit of a marginally bound particle with angular momentum per unit mass $L = 4M_{\rm BH}$. Any particle with energy $\mathcal{E} \leq 1$ and angular momentum $L \geq 4M_{\rm BH}$ has an inner turning point at $r \geq 4M_{\rm BH}$. So, a particle reaching $r = 4M_{\rm BH}$ with $\mathcal{E} = 1$ is necessarily captured by the BH [40,41]. Following [52], we model the overdensity by multiplying the DM density profile in Eqs. (10) and (13) with the cutoff factor $(1 - 4M_{\rm BH}/r)$,

The circular null geodesics satisfy the extremum condition

$$2f(r_c) = r_c f'(r_c), \tag{14}$$

which, using Eq. (6), reduces to

$$r_c = 3m(r_c). \tag{15}$$

Since the spacetime is vacuum for $r \leq 4M_{\rm BH}$, the Schwarzschild photon sphere at $r_c = 3M_{\rm BH}$ always persists. Whether additional light rings, formed as stable-unstable (inner-outer) pairs [109,110], appear or not is set not only by the global compactness $z = M_{\rm halo}/a_0$ [36,56], but also by how centrally the halo mass sits. The inner profile must be steep enough for $m(r)$ to exceed $r/3$ at some radius. If $m(r) < r/3$ throughout, no additional ring can form [36]. This bound is stronger than the dominant energy condition $[\bar{\rho} \geq \bar{p}_t(r)]$ which yields $m(r) \leq 2r/5$. A halo may therefore satisfy the latter and still develop an extra pair of light rings, in the window $1/3 < m(r)/r \leq 2/5$. However, in this narrow region, the pressure is enhanced approaching the local density. Thus, for realistic DM halo, we restrict ourself to $m(r) < r/3$, i.e., only one light ring at $r = 3M_{\rm BH}$ [56].

[1]The radius r_t for $\beta \leq 3$ is usually set to be $5a_0$.

Henceforth, for notational simplicity we will refer to the halo density profile represented by Eq. (10) with the cutoff factor $1-4M_{\rm BH}/r$ as the (α,β,γ) profile.

III. AXIAL GRAVITATIONAL PERTURBATION

With the matter distribution and background geometry specified, we study the ringdown spectrum of an asymptotically flat, static, spherically symmetric BH in a DM halo using the BH perturbation theory. We add small perturbations $h_{\mu\nu}$ to the background metric $\bar{g}_{\mu\nu}$ and the matter stress tensor, such that

$$g_{\mu\nu}=\bar{g}_{\mu\nu}+h_{\mu\nu},\qquad T_{\mu\nu}=\bar{T}_{\mu\nu}+\delta T_{\mu\nu}. \tag{16}$$

The metric perturbations and the perturbation in the fluid stress tensor are related by the linearized Einstein's equation,

$$\delta G_{\mu\nu}=8\pi\delta T_{\mu\nu}. \tag{17}$$

The perturbation of the fluid stress tensor is governed by the variation in the fluid energy density ($\delta\rho$), radial pressure δp_r, and tangential pressure δp_t, as well as the perturbation of the fluid four-velocity δu^μ and auxiliary vector δw^ν, respectively. The spherical symmetry of the background spacetime allows decomposing the metric perturbations into axial (parity-odd) and polar (parity-even) sectors depending on their behavior under the parity transformation, $\theta\to\pi-\theta$ and $\phi\to\phi+\pi$. Likewise, the perturbed energy-momentum tensor can be decomposed into the axial and polar components. In the present work, we focus solely on the axial perturbations and leave the polar sector for a future analysis.

The axial metric perturbation in the Regge-Wheeler gauge can be written as

$$h_{\mu\nu}=\begin{pmatrix}0 & 0 & h_0^{lm}(t,r)S_\theta^{lm} & h_0^{lm}(t,r)S_\phi^{lm}\\ 0 & 0 & h_1^{lm}(t,r)S_\theta^{lm} & h_1^{lm}(t,r)S_\phi^{lm}\\ \star & \star & 0 & 0\\ \star & \star & 0 & 0\end{pmatrix}, \tag{18}$$

where

$$(S_\theta^{lm},S_\phi^{lm})=\left(-\frac{1}{\sin\theta}\partial_\phi Y^{lm}(\theta,\phi),\sin\theta\partial_\theta Y^{lm}(\theta,\phi)\right) \tag{19}$$

are the vector spherical harmonics and $Y^{lm}(\theta,\phi)$ are scalar spherical harmonics with $l=2\ldots$ and $-l\le m\le l$. The $\star$ in Eq. (18) denotes the symmetric matrix components.

Interestingly, the perturbations of the fluid energy density and pressure do not contribute in the axial sector. Thus, the axial perturbation of the fluid energy-momentum tensor is solely determined by the perturbations of the fluid four-velocities δu^μ and the auxiliary vector δw^μ whose nonzero components are

$$\delta u^\theta=\frac{\sqrt{f(r)}}{4\pi(\bar{\rho}+\bar{p}_t)r^2}\sum_{l,m}U_{lm}(t,r)S_\theta^{lm}, \tag{20}$$

$$\delta u^\phi=\frac{\sqrt{f(r)}}{4\pi(\bar{\rho}+\bar{p}_t)r^2\sin^2\theta}\sum_{l,m}U_{lm}(t,r)S_\phi^{lm}, \tag{21}$$

$$\delta w^\theta=\frac{\sqrt{1-2m(r)/r}}{4\pi(\bar{\rho}+\bar{p}_t)r^2}\sum_{l,m}W_{lm}(t,r)S_\theta^{lm}, \tag{22}$$

$$\delta w^\phi=\frac{\sqrt{1-2m(r)/r}}{4\pi(\bar{\rho}+\bar{p}_t)r^2\sin^2\theta}\sum_{l,m}W_{lm}(t,r)S_\phi^{lm}. \tag{23}$$

Thus, we get the following nonzero components of the perturbed fluid stress tensor:

$$\delta T_{t\theta}=-\left(\frac{f(r)U_{lm}(t,r)}{4\pi}+h_0(t,r)\bar{\rho}(r)\right)S_\theta^{lm}, \tag{24}$$

$$\delta T_{t\phi}=-\left(\frac{f(r)U_{lm}(t,r)}{4\pi}+h_0(t,r)\bar{\rho}(r)\right)S_\phi^{lm}, \tag{25}$$

$$\delta T_{r\theta}=-\frac{\bar{p}_tW_{lm}(t,r)}{4\pi(\bar{\rho}+\bar{p}_t)}S_\theta^{lm}, \tag{26}$$

$$\delta T_{r\phi}=-\frac{\bar{p}_tW_{lm}(t,r)}{4\pi(\bar{\rho}+\bar{p}_t)}S_\phi^{lm}. \tag{27}$$

Using Eqs. (24)–(27) in Eq. (17) in cognizance with the background equations (5)–(7), we obtain the $\theta\theta$, $r\theta$, and $t\theta$ components of the perturbed Einstein equations, which constitute the governing system of differential equations in the axial sector. The $\theta\theta$ equation relates $\dot{h}_0$ with h_1 and h_1',

$$\dot{h}_0=\frac{f(r)}{r^2}[r(r-2m(r))h_1'+2(m(r)-2\pi r^3\bar{\rho}(r))h_1], \tag{28}$$

where a dot denotes derivative with respect to t and a prime denotes derivative with respect to r. The spherical symmetry of the background spacetime implies degeneracy in the azimuthal index m. Accordingly, we suppress the corresponding mode labels and omit the l subscript for notational simplicity. Defining

$$\psi=\frac{1}{r}\sqrt{f(1-2m(r)/r)}h_1 \tag{29}$$

and substituting Eq. (28) in the $r\theta$ equation, we get the sourced Regge-Wheeler equation as

$$\frac{d^2\psi}{dr_*^2}-\frac{d^2\psi}{dt^2}-V(r)\psi=\frac{4f(r)m(r)\sqrt{f(r)(1-2m(r)/r)}}{r(2r-3m(r))}W, \tag{30}$$

where

$$V(r)=f(r)\left(\frac{l(l+1)}{r^2}+\frac{4\pi r\rho(r)}{r-2m(r)}-\frac{6m(r)}{r^3}\right) \tag{31}$$

is the effective potential and r_* is the tortoise coordinate, defined as $\frac{dr_*}{dr}=1/\sqrt{f(r)(1-2m(r)/r)}$. The $t\theta$ equation, on the other hand, yields

$$\left(1-\frac{2m(r)}{r}\right)\left[h_0''-\dot{h}_1'-\frac{2}{r}\dot{h}_1\right]-4\pi r(h_0'-\dot{h}_1)\bar{\rho}(r) -\left[\frac{l(l+1)}{r^2}-\frac{4m(r)}{r^3}+\frac{r-m(r)}{r-2m(r)}8\pi\rho(r)\right]h_0=4f(r)U(t,r). \tag{32}$$

However, we still need one more equation to close the system as we have four unknown functions, namely, h_0, h_1, U, and W. To this end, we choose the fluid four-velocity u^μ to be irrotational (zero vorticity) [56,95],

$$\omega^\mu=\epsilon^{\mu\nu\alpha\beta}u_\nu\nabla_\alpha u_\beta=0. \tag{33}$$

Equation (33) leads to the following expression for $U(t,r)$:

$$U(t,r)=-\frac{4\pi h_0(t,r)}{f(r)}[\bar{p}_t(r)+\bar{\rho}(r)]. \tag{34}$$

From Eq. (34), it follows that the covariant fluid-velocity perturbation vanishes, i.e., $\delta u_\mu=0$. We emphasize that the contravariant components do not vanish: $\delta u^\theta,\delta u^\phi\propto U\neq 0$ by Eqs. (20) and (21), so the fluid does acquire an axial velocity. What vanishes is the combination $\delta u_\mu=\bar{g}_{\mu\nu}\delta u^\nu+h_{\mu\nu}\bar{u}^\nu$, in which the fluid motion is exactly compensated by the frame dragging of the axial metric perturbation. Substituting Eq. (34) in the θ component of the linearized version the conservation equation $\nabla_\mu T^{\mu\nu}$,

$$\left[\frac{\partial}{\partial r}+\frac{B(r)}{A(r)}\right][W+4\pi h_1(\bar{p}_t+\bar{\rho})]=0, \tag{35}$$

where

$$A(r)=2r^4m-11r^3m^2+20r^2m^3-12rm^4, \tag{36}$$

$$B(r)=2r^3m-10r^2m^2+18rm^3-12m^4+8\pi r^6\bar{\rho} -40\pi r^5m\bar{\rho}+60\pi r^4m^2\bar{\rho}-24\pi r^3m^3\bar{\rho}. \tag{37}$$

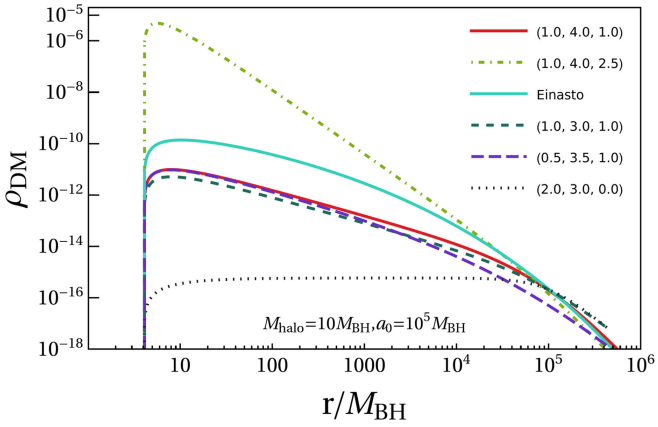


FIG. 1. Plot showing the shape of the DM density profile for different values of the shape parameter (α,β,γ) for a halo of total mass $10M_{BH}$ with $a_0=10^5M_{BH}$. In particular, we consider Hernquist (1, 4, 1), generalized Dehnen (1, 4, 2.5), Navarro-Frenk-White (NFW) (1, 3, 1), Dekel-Zhao (0.5, 3.5, 1), and King (2, 3, 0) profiles. The Einasto density distribution with the same halo mass and compactness is also shown for comparison.

It is obvious that one solution of Eq. (35) is

$$W=-4\pi h_1(\bar{p}_t+\bar{\rho}). \tag{38}$$

The choice Eq. (38) is equivalent to the condition $\delta w_\mu=0$ and is therefore a statement about the perturbed matter configuration. This in turn transforms Eq. (30) to the source-free Schrödinger-like form [56,95]

$$\frac{d^2\psi}{dr_*^2}-\frac{d^2\psi}{dt^2}-V(r)\psi=0, \tag{39}$$

with the effective potential [51,53,94]

$$V(r)=f(r)\left(\frac{l(l+1)}{r^2}-\frac{6m(r)}{r^3}+\frac{m'(r)}{r^2}\right). \tag{40}$$

In the limit of vanishing halo density, Eq. (39) reduces to the standard Regge-Wheeler equation for a Schwarzschild BH [111]. From Fig. 2, we observe that, while the qualitative structure of the effective potential remains unchanged by the presence of the DM halo, quantitative deviations arise that depend on the halo compactness $(z=M_{halo}/a_0)$, the inner logarithmic slope γ, the outer logarithmic slope β, and the transition parameter α.

IV. RINGDOWN SPECTRA: FREQUENCY-DOMAIN ANALYSIS

Having specified the background spacetime and derived the perturbation equations, we now examine how the surrounding DM distribution modifies the ringdown spectrum of the BH.

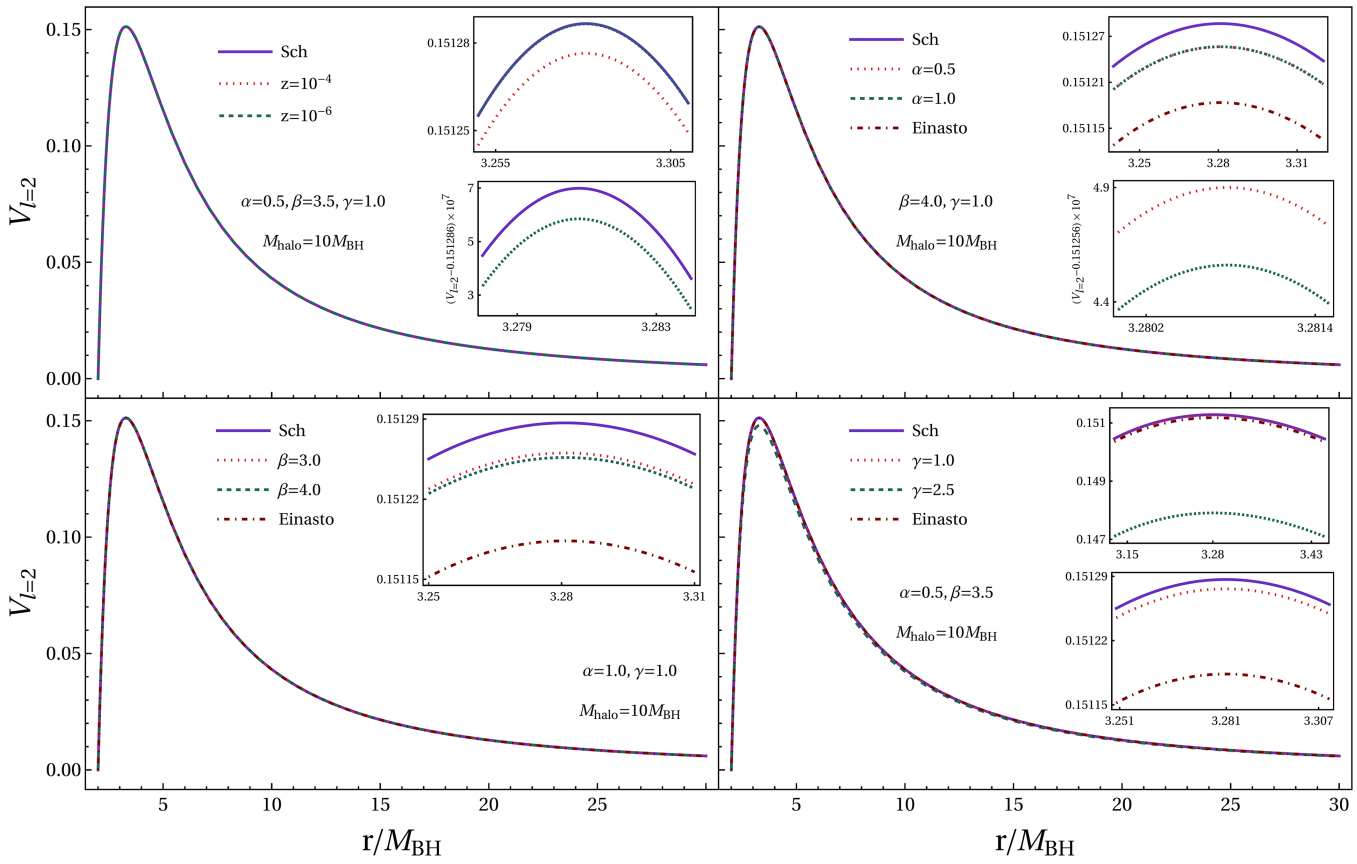


FIG. 2. Effective potential in the axial sector for the $l = 2$ mode for different choices of the halo parameters: (top left) compactness z, (top right) α, (bottom left) β, and (bottom right) γ. In each panel, the solid blue curve denotes the Schwarzschild effective potential. The top-right and bottom panels also include the effective potential for an Einasto-type DM halo. The inset in each panel shows a magnified view of the potential near its peak. For top-left plot, a_0 is $10^5 M_{\rm BH}$ when $z = 10^{-4}$ and $a_0 = 10^7 M_{\rm BH}$ when $z = 10^{-6}$. In remaining panels, $a_0 = 10^5 M_{\rm BH}$ and $z = 10^{-4}$.

We use a sixth-order WKB approximation method [59], which extends the original formulation of Schutz and Will [58] and Iyer and Will [57]. We start by separating the radial and temporal dependence of ψ as

$$\psi(t, r) = \psi(r) \exp(-i\omega t), \tag{41}$$

and we rewrite Eq. (39) in the Schrödinger-like form

$$\frac{d^2\psi(r)}{dr_*^2} + Q(r_*)\psi(r) = 0, \tag{42}$$

where

$$Q(r_*) = \omega^2 - V(r_*). \tag{43}$$

The WKB solutions are then matched across the two classical turning points of the effective potential barrier, leading to the quantization condition

$$i\frac{Q_0}{\sqrt{2Q_0''}} - \sum_{k=2}^{6} \Lambda_k = n + \frac{1}{2}, \qquad n = 0, 1, \ldots \tag{44}$$

where Q_0 and Q_0'' denote Q and its second derivative evaluated at the maximum of the effective potential, and Λ_k represent higher-order correction terms determined by higher derivatives of the potential at the same point. The fundamental mode corresponds to $n = 0$, the first overtone corresponds to $n = 1$, and so on. The sixth-order corrections substantially improve the accuracy of the WKB approximation and for $l > n$ achieves an accuracy comparable to Leaver's method [112].[2]

[2]In [53], the authors computed the QNM frequencies of a static spherically symmetric BH surrounded by a Hernquist and NFW-type DM halo, with the inner cutoff radius at $r = 2M_{\rm BH}$ using a generalized matrix method. However, introducing a realistic inner cutoff radius at $r = 4M_{\rm BH}$ and varying the halo parameters, we observe that a large number of grid points ($N \gg 17$) are required for the QNMs to converge with accuracy comparable to that of sixth-order WKB method. This greatly increases computational cost, limiting the applicability of the method in the present study.

A. Light ring and eikonal QNMs

Before presenting the QNM spectrum, we analyze the properties of the unstable circular null geodesic (light ring). In the eikonal limit, the real and imaginary parts of the QNM frequencies are determined by the light ring angular frequency Ω_c and the corresponding Lyapunov exponent λ_c, respectively. We therefore investigate the dependence of these quantities on the DM halo parameters and use the resulting behavior to interpret the QNM spectrum discussed below.

The angular frequency of the light ring located at $r = r_c$ is

$$\Omega_c = \frac{\sqrt{f(r_c)}}{r_c}, \tag{45}$$

while the principal Lyapunov exponent, which characterizes the instability timescale of the circular null orbit, is [61]

$$\lambda_c = \frac{1}{\sqrt{2}}\sqrt{-\frac{r_c^2}{f(r_c)}\left(\frac{d^2}{dr_*^2}\frac{f(r)}{r^2}\right)_{r=r_c}}. \tag{46}$$

To quantify the halo-induced deviations, we define the fractional shifts from the corresponding Schwarzschild values,

$$\delta\Omega_c = 1 - \frac{\Omega_c^{\rm DM}}{\Omega_c^{\rm Sch}}, \qquad \delta\lambda_c = 1 - \frac{\lambda_c^{\rm DM}}{\lambda_c^{\rm Sch}}. \tag{47}$$

The last columns of Figs. 4–6 show $\delta\Omega_c$ and $\delta\lambda_c$ as functions of γ, β, and α, respectively, for two representative compactnesses $z = M_{\rm halo}/a_0 = (10^{-6}, 10^{-4})$. For a given halo model, both $\delta\Omega_c$ and $\delta\lambda_c$ increase with halo compactness, indicating larger deviations from the Schwarzschild values as the halo becomes more compact, consistent with the findings of [53].

Although the DM distribution begins only at $r = 4M_{\rm BH}$, well outside the light ring at $r_c = 3M_{\rm BH}$, the halo still redshifts Ω_c and λ_c through its cumulative effect on $f(r_c)$. We show in Appendix A that this redshift is exact,

$$f(r_c) = \frac{1}{3}e^{-\mathcal{I}}, \tag{48}$$

giving the compact form

$$\Omega_c = \Omega_c^{\rm Sch} e^{-\mathcal{I}/2}, \tag{49}$$

where the halo integral

$$\mathcal{I} \equiv \int_{4M_{\rm BH}}^{\infty} \frac{2m_h(r)}{[r-2m(r)][r-2M_{\rm BH}]}\,dr > 0 \tag{50}$$

encodes the full nonlinear effect of the halo mass distribution $m_h(r) = m(r) - M_{\rm BH}$, so that $\delta\Omega_c = 1 - e^{-\mathcal{I}/2}$. A further exact result, also derived in Appendix A, is that the local geometry at r_c is unaffected by the halo profile, so that λ_c acquires exactly the same redshift factor as Ω_c,

$$\lambda_c = \Omega_c = \Omega_c^{\rm Sch} e^{-\mathcal{I}/2}, \tag{51}$$

$$\delta\Omega_c = \delta\lambda_c = 1 - e^{-\mathcal{I}/2}, \tag{52}$$

valid for any (α, β, γ) profile. This identity is confirmed numerically by the overlapping of $\delta\Omega_c$ and $\delta\lambda_c$ in the right panels of Figs. 4–6. It may be noted that for dilute halos (small z) with shallow inner logarithmic slope (low γ), Eq. (51) can be written in a form similar to Eqs. (19) and (20) of [53].

Even at fixed compactness, both Ω_c and λ_c depend clearly on the shape of the underlying density profile, with the strongest variation arising from the inner logarithmic parameter γ, followed by β and then α, as seen in Figs. 4–6. This ordering follows from how each parameter redistributes halo mass relative to the radial weight $(r - 2M_{\rm BH})^{-1}$ entering $\mathcal{I}$, which is largest near the inner cutoff. Increasing γ moves mass inward most efficiently and so dominates the redshift, β acts more uniformly across all radii, and α only redistributes mass over the comparatively gentle transition region near a_0. Appendix A derives this mechanism in detail and identifies the regimes in which the ordering can change, including a sign reversal in the α dependence at small γ.

In vacuum general relativity, the QNM frequencies in the eikonal limit ($l \gg 1$) are related to the light ring parameters through

$$\omega_c = l\Omega_c - i\left(n + \frac{1}{2}\right)|\lambda_c|, \tag{53}$$

where l and n denote the angular and overtone numbers, respectively. In the axial sector, where fluid modes are absent, this correspondence is expected to remain approximately valid. Using Eq. (51), the eikonal frequencies take the compact form

$$\omega_c = \Omega_c^{\rm Sch} e^{-\mathcal{I}/2}\left[l - i\left(n + \frac{1}{2}\right)\right], \tag{54}$$

so both $\mathrm{Re}\,\omega_c$ and $\mathrm{Im}\,\omega_c$ are redshifted by the same factor $e^{-\mathcal{I}/2}$ relative to their Schwarzschild values. Since $\mathcal{I}$ depends on the full profile shape (α, β, γ) and not merely on $M_{\rm halo}$, halos with identical mass and compactness but different density profiles generally produce different values of $\mathcal{I}$ and hence distinct ringdown signatures. This same profile dependence, however, also makes different halo configurations capable of producing an identical shift, a steep inner cusp at low compactness can mimic a shallower

cusp at higher compactness, represented by the horizontal line in the right panel of Fig. 4, whose intersections give two halo configurations with different compactness and inner cusp but the same Ω_c and λ_c. We return to this degeneracy in Appendix A.

Appendix A provides a complete analytic derivation of the results summarized in this section. We also compare in Table II the frequencies predicted by the eikonal relation Eq. (54) with those obtained from the sixth-order WKB approximation for several representative halo models at fixed compactness.

B. Effect of halo parameters on QNMs

To systematically quantify the influence of the halo parameters on the ringdown spectrum, we compute the fractional deviations (redshift) of the real and imaginary parts of the quasinormal mode frequencies from their corresponding Schwarzschild values for a given multipole and overtone,

$$\delta\omega_{\mathrm{Re/\,Im}} = \frac{\omega^{\mathrm{Sch.}}_{\mathrm{Re/\,Im}} - \omega^{\mathrm{DM}}_{\mathrm{Re/\,Im}}}{\omega^{\mathrm{Sch.}}_{\mathrm{Re/\,Im}}}. \tag{55}$$

Motivated by the dependence of the eikonal frequencies on the halo compactness, we show in Fig. 3 the variation of $\delta\omega_{\mathrm{Re}}$ and $\delta\omega_{\mathrm{Im}}$ with compactness for several representative halo models. We find that, for a fixed density profile, increasing halo compactness leads to progressively larger deviations of both the QNM frequency and damping rate from their Schwarzschild values. The fractional deviations at the leading order are linear in compactness. This is explicitly shown by the linear fit in Fig. 3 and is in agreement with the observations of [53]. The fractional deviations in the real and imaginary parts of ω remain nearly identical for all halo profiles and compactnesses considered. This behavior is a direct consequence of the common halo redshift mechanism derived in Appendix B, with the small residual differences reflecting higher-order corrections beyond the analytic approximation. The horizontal lines constitute the degeneracy surface, showing that the same QNM value can be obtained from DM profiles with different compactness and shape parameters. To highlight the dependence of the fractional redshift on the detailed shape parameters of the DM profile, we plot $\delta\omega_{\mathrm{Re/\,Im}}$ for the fundamental $l = 2$ mode and its first overtone against γ, β, and α in the first two columns of Figs. 4–6, respectively. The redshift grows with both the inner logarithmic slope γ and the outer logarithmic slope β, with γ dominating over most of the parameter space explored. This ordering is not universal, however, for small γ or a small gap $\beta - \gamma$, the sensitivity to β can match or exceed that of γ, as seen in the upper panels of Figs. 4 and 5. The dependence on the transition parameter α is more subtle still and changes sign with γ. Figure 6 shows the redshift increasing with α at $\gamma = 1.0$ (top row), but decreasing with α at $\gamma = 2.5$ (middle and bottom rows), with the crossover occurring near $\gamma \approx 1$. Appendix B derives the radial mechanism behind each of these trends and identifies precisely where the orderings hold and where they invert. The physical constraint $\beta > \gamma$ also bounds how large the redshift can become at fixed β and M_{halo}. As $\gamma \to \beta^-$, the profile approaches a single power law and $\delta\omega$ saturates at a finite value $\delta_{\mathrm{sat}}(\beta, M_{\mathrm{halo}})$, shared by both the eikonal and noneikonal quantities, rather than increasing without bound. We derive this saturation value explicitly in Appendix B. A finite saturation means that, for a given $(\beta, M_{\mathrm{halo}})$, there is a maximum redshift reachable by varying γ alone. A measured $\delta\omega$ above $\delta_{\mathrm{sat}}(\beta, M_{\mathrm{halo}})$ would be inconsistent with the (α, β, γ) family at that halo mass, giving a direct observational constraint, while a measured shift below δ_{sat} remains consistent with a range of γ values and feeds into the degeneracy discussed below. Because δ_{sat} depends on M_{halo} rather than on a_0 individually, this bound constrains γ once $(\beta, M_{\mathrm{halo}})$ are otherwise fixed or independently known, regardless of a_0. In Fig. 7, we plot the variation of $\delta\omega_{\mathrm{Re/\,Im}}$ with γ for different compactness at fixed α and β.

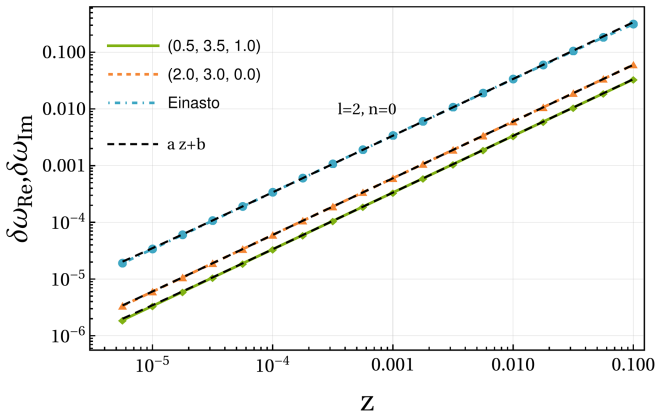


FIG. 3. Fractional deviation in the real QNM frequency and damping rate from the corresponding Schwarzschild values with compactness for three halo configurations as depicted in the plot with $a_0 = 10^5 M_{\mathrm{BH}}$. The deviation in the real oscillation frequency is represented by distinct line styles (solid, dashed, dot-dashed), while the corresponding deviation in the damping rate is displayed as discrete points. The black dashed line represents a linear fit.

Note that unlike Figs. 4–6, where the compactness is varied by changing a_0 at fixed M_{halo}, the compactness in Fig. 7 is varied by changing M_{halo} at fixed a_0. The two choices are not equivalent away from small compactness. As γ approaches its maximum value β, the curves in Fig. 4 converge to a common value regardless of a_0, whereas the curves in Fig. 7 remain separated according to M_{halo}, since the saturated redshift depends on M_{halo} but not on a_0 individually (see Appendix B for the underlying argument). For $\gamma \lesssim 1$, we observe that the QNM shifts can be expressed

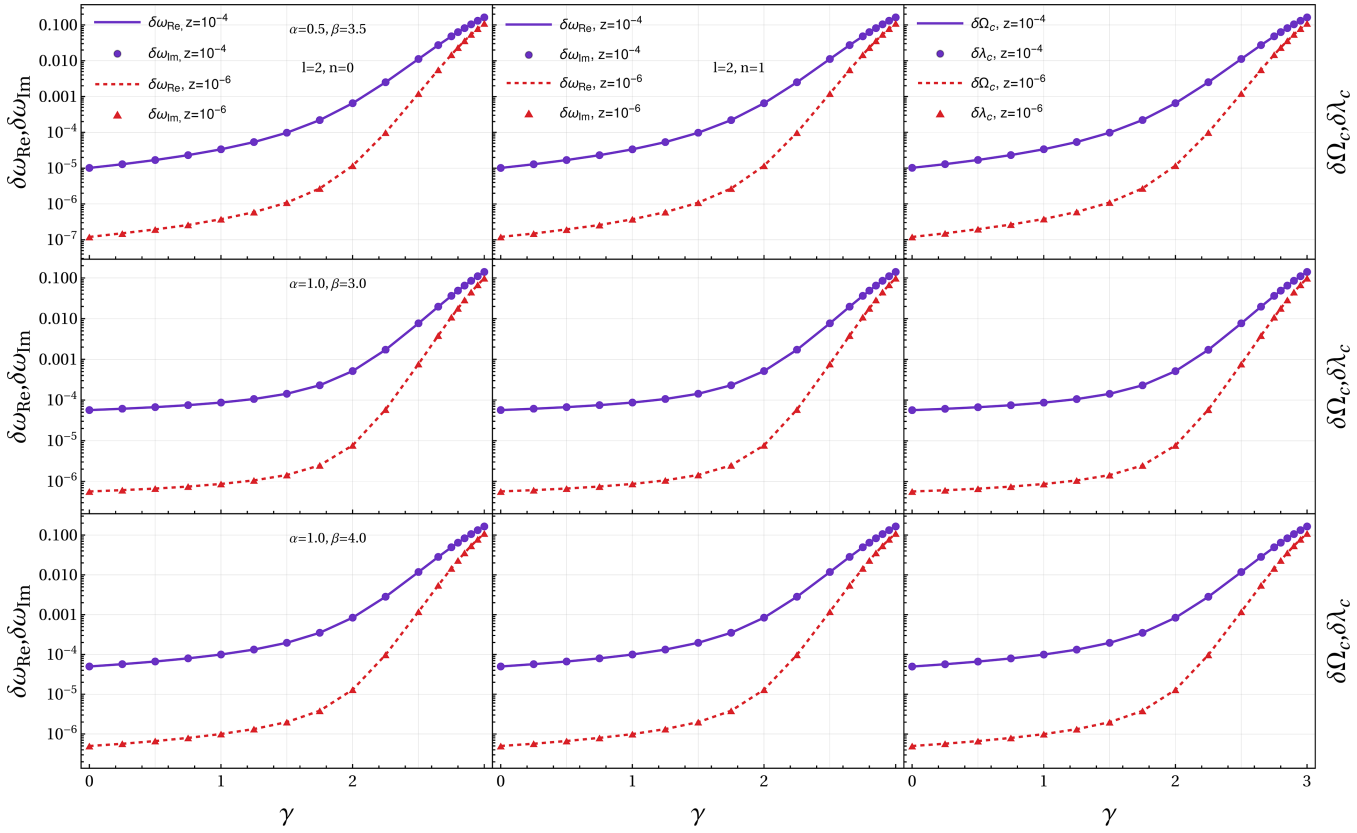


FIG. 4. Fractional deviations from Schwarzschild values, plotted on a logarithmic scale, as functions of the halo parameter γ. In each panel, the upper and lower curves correspond to compactness values $z = 10^{-4}$ and 10^{-6}, respectively. When $z = 10^{-4}$, we took $a_0 = 10^5 M_{\rm BH}$ and for $z = 10^{-6}$, we set $a_0 = 10^7 M_{\rm BH}$, leading to a constant $M_{\rm halo} = 10 M_{\rm BH}$ in both of the cases. The first and second columns show the fractional deviations in the oscillation frequency and damping rate of the $l = 2$ fundamental ($n = 0$) and first-overtone ($n = 1$) QNMs, respectively. Fractional deviation of the real oscillation frequency is represented by distinct line styles (solid, dashed), while fractional deviation in the damping rate is displayed as discrete points. The third column shows the corresponding fractional deviations in the light ring angular frequency and the principal Lyapunov exponent. Fractional deviation in the light ring angular frequency is also represented by distinct line styles (solid, dashed), while fractional deviation in the principal Lyapunov exponent is displayed as discrete points. Each row corresponds to a fixed α and β as depicted in the plot.

as a polynomial, $\delta\omega \approx \sum_{i\geq 0} a_i \gamma^i$, however, at larger γ the polynomial dependence breaks down as the growth accelerates (see Appendix B 3). This is explicitly shown in Fig. 7 by the polynomial fit of $\delta\omega_{\rm Re/\,Im}$ for $\gamma \leq 1$.

These trends closely mirror those observed for the fractional shifts in the light ring frequency and principal Lyapunov exponent, providing further support for the eikonal interpretation of the quasinormal mode spectrum. We provide a detailed analysis in Appendix B.

The strong localization of the redshift kernel near the inner cutoff naturally raises the question of how sensitive the predicted QNM shifts are to the choice of the inner truncation radius, r_0. Figure 8 addresses this issue by comparing the fundamental $(\ell = 2, n = 0)$ oscillation frequency and damping rate obtained using the horizon cutoff $r_0 = 2M_{\rm BH}$, standard in the literature [53], and our value $r_0 = 4M_{\rm BH}$ (see also [113]). For small γ, the difference between the two is less than 10^{-7}. As γ increases, the corresponding difference between $2M_{\rm BH}$ and $4M_{\rm BH}$ grows, and the difference rises to 0.1 by $\gamma = 3$. The cutoff is thus a physical choice in the cuspy regime, not a convention, and $r_0 = 4M_{\rm BH}$ is the appropriate one, since matter crossing it is captured [41].

C. Observational relevance of the halo-induced QNM shifts

We now place the halo-induced QNM shifts in the context of present observational precision. The purpose of this comparison is not to derive a direct observational bound on the DM halo parameters, since our calculation describes axial perturbations of a static, spherically symmetric BH embedded in a prescribed matter distribution. The available observational constraints, by contrast, are obtained from binary BH merger data using waveform models for a Kerr remnant. Nevertheless, the precision achieved in current BH spectroscopy provides a useful benchmark for judging the magnitude of the environmental shifts predicted in this work.

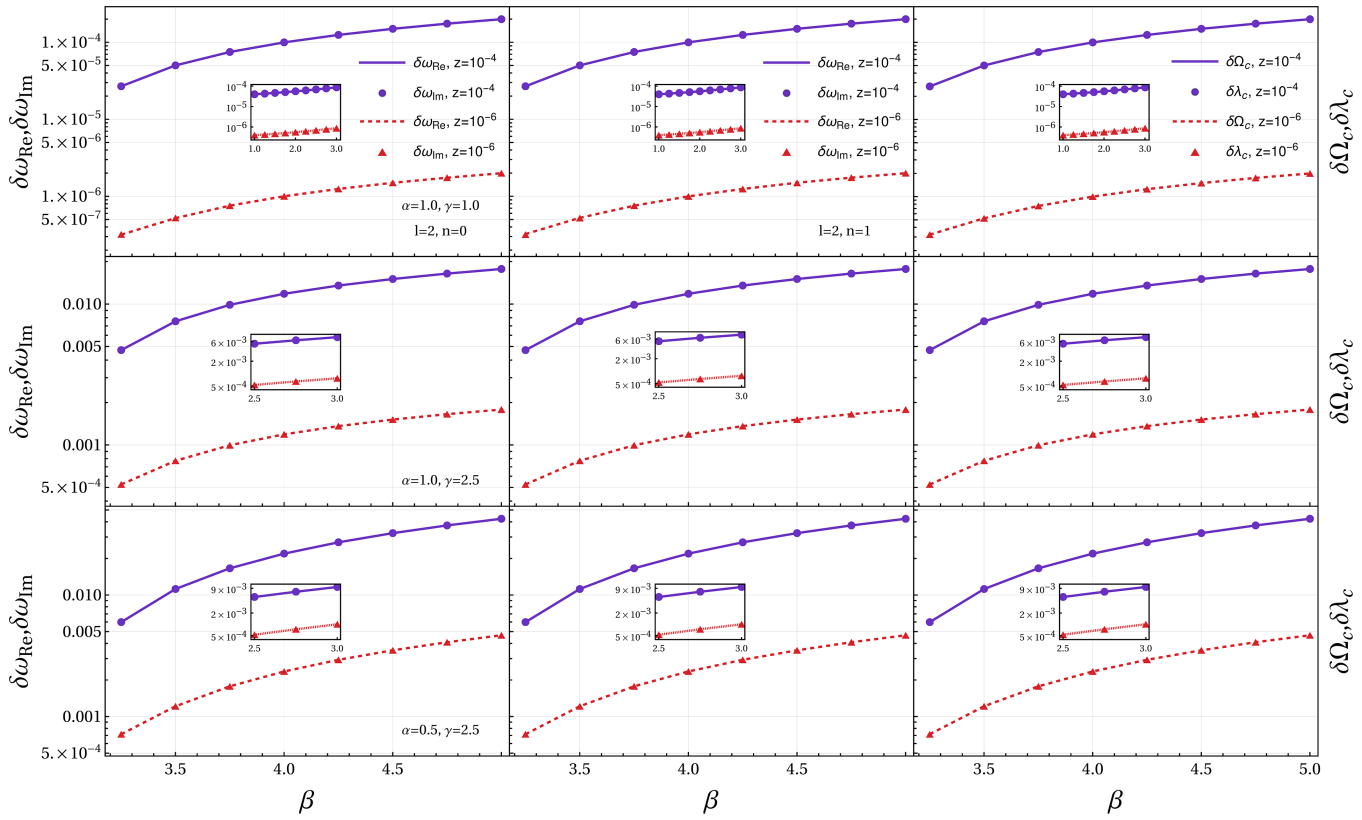


FIG. 5. Fractional deviations from Schwarzschild values, plotted on a logarithmic scale, as functions of the halo parameter β. In each panel, the upper and lower curves correspond to compactness values $z = 10^{-4}$ and 10^{-6}, respectively. When $z = 10^{-4}$, we took $a_0 = 10^5 M_{\rm BH}$ and for $z = 10^{-6}$, we set $a_0 = 10^7 M_{\rm BH}$, leading to a constant $M_{\rm halo} = 10 M_{\rm BH}$ in both of the cases. The first and second columns show the fractional deviations in the oscillation frequencies and damping rates of the $l = 2$ fundamental ($n = 0$) and first-overtone ($n = 1$) QNMs, respectively. The third column shows the corresponding fractional deviations in the light ring angular frequency and the principal Lyapunov exponent. The inset in each panel shows the corresponding quantities on a logarithmic scale for small values of β. Each row corresponds to a fixed α and γ as depicted in the plot.

We use as reference the recent LVK analysis of GW250114, which provides one of the strongest single-event tests of the Kerr ringdown spectrum [114,115]. In that analysis, the oscillation frequency and damping time of the fundamental mode are parametrized as

$$f_{\ell m 0} = f^{\rm GR}_{\ell m 0}\left(1+\delta\hat{f}_{\ell m 0}\right), \quad \tau_{\ell m 0} = \tau^{\rm GR}_{\ell m 0}(1+\delta\hat{\tau}_{\ell m 0}). \tag{56}$$

The general relativity (GR) values are computed from the remnant mass and spin inferred from the full inspiral-merger-ringdown signal. For the dominant (2, 2, 0) mode, the reported constraints are

$$\delta\hat{f}_{220} = 0.02^{+0.02}_{-0.02}, \qquad \delta\hat{\tau}_{220} = -0.01^{+0.10}_{-0.09}, \tag{57}$$

at the 90% credible level. These intervals are consistent with the Kerr prediction within the present measurement uncertainty.

In the present work, we characterize the QNM spectrum in terms of the complex frequency

$$\omega = \omega_{\rm Re} - i\omega_{\rm Im}, \tag{58}$$

where the imaginary part determines the damping time through

$$\omega_{\rm Im} = \frac{1}{\tau}. \tag{59}$$

The fractional shifts used throughout this work are defined as

$$\delta\omega_{\rm Re/\,Im} = \frac{\omega^{\rm Sch}_{\rm Re/\,Im} - \omega^{\rm DM}_{\rm Re/\,Im}}{\omega^{\rm Sch}_{\rm Re/\,Im}}. \tag{60}$$

With this convention, a positive halo-induced redshift corresponds to a lower oscillation frequency and a longer damping time. To linear order in the fractional deviation, the two conventions are related by

$$\delta\omega_{\rm Re} \simeq -\delta\hat{f}, \qquad \delta\omega_{\rm Im} \simeq \delta\hat{\tau}. \tag{61}$$

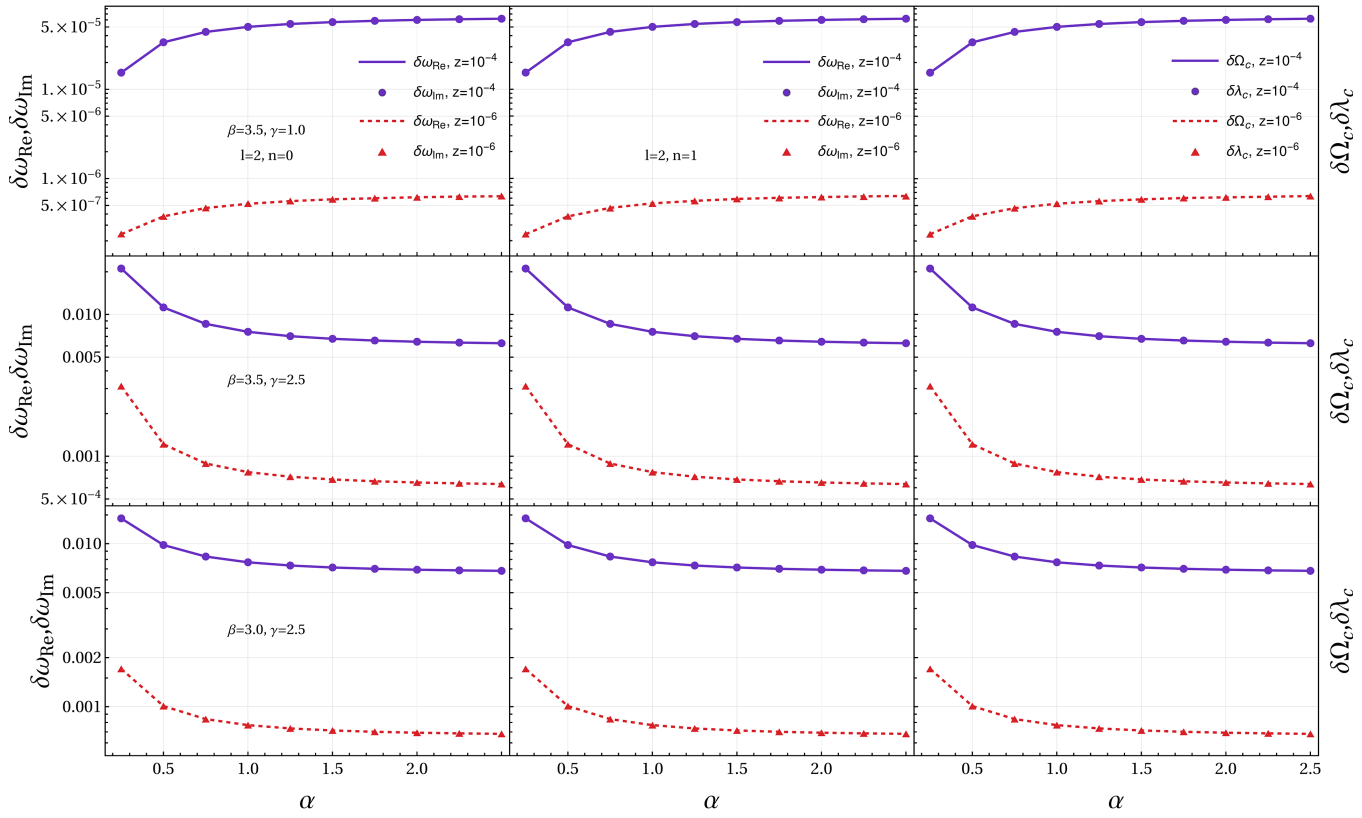


FIG. 6. Fractional deviations from Schwarzschild values, plotted on a logarithmic scale, as functions of the halo parameter α. In each panel, the upper and lower curves correspond to compactness values $z = 10^{-4}$ and 10^{-6}, respectively. When $z = 10^{-4}$, we took $a_0 = 10^5 M_{\rm BH}$ and for $z = 10^{-6}$, we set $a_0 = 10^7 M_{\rm BH}$, leading to a constant $M_{\rm halo} = 10 M_{\rm BH}$ in both of the cases. The first and second columns show the fractional deviations in the oscillation frequency and damping rate of the $l = 2$ fundamental ($n = 0$) and first-overtone ($n = 1$) QNMs, respectively. The third column shows the corresponding fractional deviations in the light ring angular frequency and the principal Lyapunov exponent. Each row corresponds to a fixed β and γ as depicted in the plot.

We therefore use

$$|\delta\omega_{\rm Re}| \sim 0.04, \qquad |\delta\omega_{\rm Im}| \sim 0.09 \tag{62}$$

as representative reference values for the current precision with which the real and imaginary parts of the dominant QNM frequency can be tested.

Figure 11 compares these reference values with the fractional shifts predicted by our halo models at fixed compactness $z = 10^{-4}$. The shifts grow monotonically with the inner logarithmic slope γ, showing that centrally concentrated halos produce larger changes in the ringdown spectrum. For the representative profiles shown in the figure, only sufficiently cuspy configurations lead to shifts comparable to the present benchmark precision. Standard profiles such as NFW-like or Hernquist-like profiles remain below this level for the chosen compactness and would therefore be difficult to distinguish from the vacuum Schwarzschild prediction using a measurement of comparable precision.

We next examine the full (α, β, γ) parameter space. In Figs. 9 and 10, we vary the parameters, such that

$$\alpha \in [0.25, 2.5], \qquad \beta \in [0.25, 5], \qquad \gamma \in [0, 3], \tag{63}$$

and retain only the physically allowed region satisfying $\beta \geq \gamma$. The colored surface marks the locus where the predicted QNM shift becomes comparable to the observational reference precision. Points lying on the side of the surface with larger redshift correspond to halo configurations that would produce a potentially resolvable departure from the Schwarzschild value in an observation of similar quality. Points on the other side remain within the present measurement uncertainty.

The comparison between Figs. 9 and 10 shows the expected compactness dependence. At $z = 10^{-4}$, a larger portion of the physically allowed parameter space can produce shifts near the reference precision. At $z = 10^{-6}$, the corresponding region shrinks substantially, and only very centrally concentrated profiles remain capable of producing comparable deviations. This confirms that the

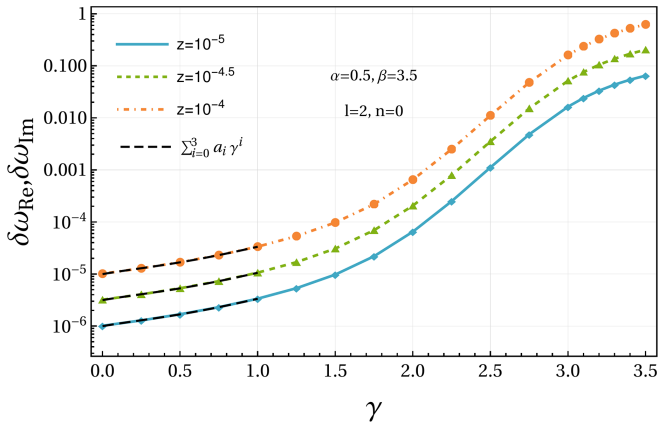


FIG. 7. Degeneracy in the fractional deviations of the QNM frequencies from Schwarzschild values across different combinations of compactness (z) and inner logarithmic slope (γ) with $a_0 = 10^5 M_{\rm BH}$. The horizontal grid lines, which intersect any two or three curves, explicitly illustrate the parametric degeneracy in which distinct physical configurations (z, γ) yield same QNM frequencies. Fractional deviation of the real oscillation frequency is represented by distinct line styles (solid, dashed, dot-dashed), while fractional deviation in the damping rate is displayed as discrete points. The black dashed line denotes a polynomial fit to the fractional deviation for $\gamma \in [0, 1]$. Here a_0 has fixed value of $10^5 M_{\rm BH}$.

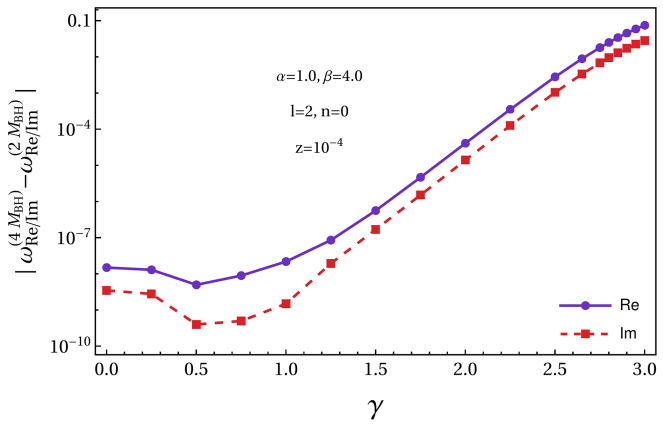


FIG. 8. Difference in the fundamental ($l = 2$, $n = 0$) QNM oscillation frequency and damping rate computed using halo profiles with inner cutoffs at $2M_{\rm BH}$ and $4M_{\rm BH}$. The figure shows the magnitude of the differences on a logarithmic scale.

observational relevance of the effect is controlled jointly by the halo compactness and the profile shape, with the inner logarithmic slope γ playing the dominant role in the parameter range considered here.

A direct observational constraint would require waveform models that consistently include the environmental modification throughout the inspiral, merger, and ringdown. The present analysis instead shows that, if future massive BH or extreme-mass-ratio systems are observed with comparable or better ringdown precision, sufficiently compact and

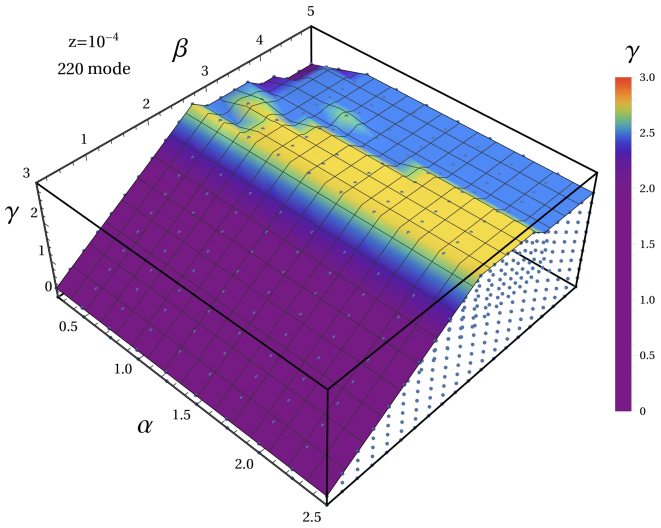


FIG. 9. Three-dimensional parameter space of the generalized (α, β, γ) halo profile for compactness $z = 10^{-4}$ and $a_0 = 10^5 M_{\rm BH}$. Only the physically allowed region satisfying $\beta \geq \gamma$ is shown. The colored surface corresponds to parameter combinations for which the predicted fractional deviations in the oscillation frequency and damping rate of the $l = 2$ fundamental QNM become comparable to the representative 90% credible intervals inferred from GW250114.

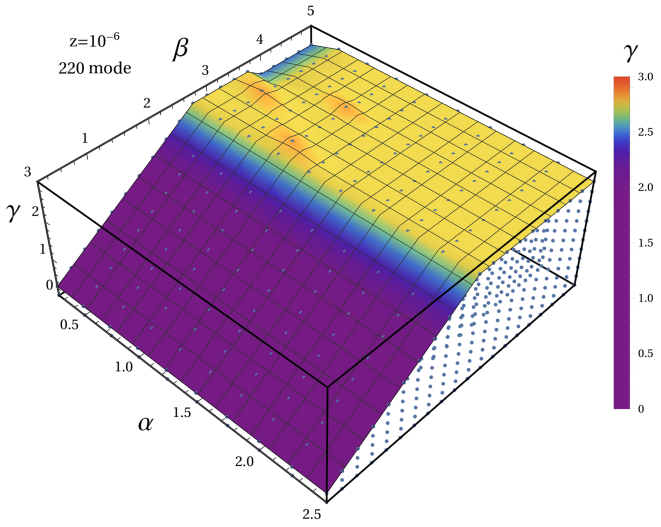


FIG. 10. Three-dimensional parameter space of the generalized (α, β, γ) halo profile for compactness $z = 10^{-6}$ and $a_0 = 10^7 M_{\rm BH}$. Only the physically allowed region satisfying $\beta \geq \gamma$ is shown. The colored surface corresponds to parameter combinations for which the predicted fractional deviations in the oscillation frequency and damping rate of the $l = 2$ fundamental QNM become comparable to the representative 90% credible intervals inferred from GW250114.

cuspy DM environments could produce QNM shifts large enough to be observationally relevant. Conversely, shallow or weakly compact halos are expected to remain degenerate with the vacuum prediction at current precision.

V. TIME-DOMAIN ANALYSIS

The frequency-domain WKB results of the preceding section provide accurate quasinormal frequencies for $l > n$, but cannot access the late-time behavior of the signal or the transient structure that connects the ringdown to the power-law tail. Thus, to complement the frequency-domain analysis and to verify the late-time behavior predicted in [116], we solve the master equation (39) directly in the time domain using the characteristic integration scheme of Gundlach *et al.* [60]. The evolution is initiated by a Gaussian pulse, whose scattering off the effective potential barrier generates the characteristic sequence of prompt response, quasinormal ringing, and late-time tail. The late-time tail and quasinormal ringing arise from distinct physical mechanisms. While quasinormal ringing is produced by resonant scattering off the effective potential barrier, the late-time tail originates from the backscattering of long-wavelength perturbations by the asymptotic spacetime curvature. For generic compact initial data with multipolar index l, the perturbation at fixed spatial position decays following Price law [60] at the leading order [117]

$$\psi \propto t^{-(2l+3)} \tag{64}$$

at asymptotically late times. This power-law behavior arises from the branch-cut contribution of the frequency-domain Green's function and is therefore governed by the asymptotic behavior of the effective potential rather than its near-horizon structure. In the presence of a fluid (including DM) environment around the central BH, the perturbation of the surrounding fluid excites the fluid modes which appear in the time-domain signal after the prompt-ringdown phase. Such fluid driven modes have been explicitly shown to be excited in the polar sector [50,118]. In the axial sector (with $\delta u_\mu = \delta w_\mu = 0$), however, the time evolution of the perturbation is governed by the source-free Schrödinger-like equation (39), where the effective potential takes the asymptotic form,

$$V_\infty(r) \approx \frac{l(l+1)}{r^2} - 2(M_{\rm BH} + M_{\rm halo})\frac{l(l+1)+3}{r^3} + 4\pi C_\beta \frac{\beta+3}{\beta-3} r^{-\beta} + \mathcal{O}\left(r^{-\mathrm{Min}[(\beta+\alpha),4]}\right), \tag{65}$$

where $C_\beta = \bar{\rho}_0 a_0^\beta$. Thus, for $\beta > 3$ the DM contributions vanish faster than $1/r^2$ at large r and consequently the late-time tail decays as $t^{-(2l+3)}$ [116]. For $\beta \leq 3$, the halo mass diverges at large r, thus the halo is truncated at a tidal radius $r_t > a_0$. This causes an observer at $r_t > r_{\rm obs} > a_0$ ($a_0 \gg M_{\rm BH}$) to witness a shallower falloff at intermediate time, $a_0 < t < r_t$,

$$\psi(t) \propto t^{-(2l+\beta)}. \tag{66}$$

Beyond the truncation radius, where the spacetime becomes Schwarzschild (with an enhanced ADM mass

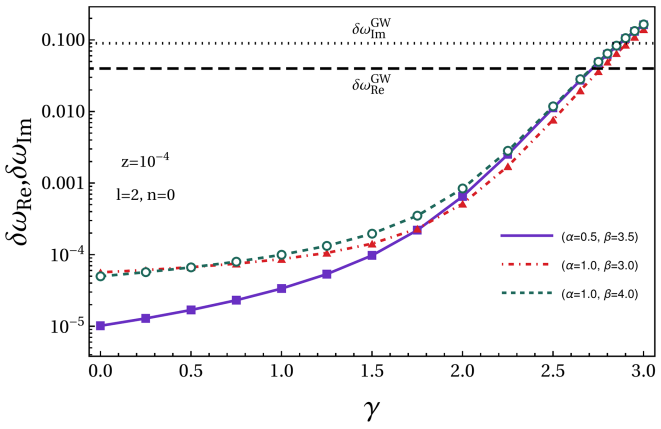


FIG. 11. Comparison of the predicted fractional QNM deviations for representative halo profiles with compactness $z = 10^{-4}$ and $a_0 = 10^5 M_{\rm BH}$ with the current observational precision inferred from GW250114. The black dashed and dotted lines denote the representative 90% credible intervals for the real and imaginary parts of the $l = 2$ fundamental QNM frequency, respectively. The fractional deviations in the real part are shown by colored curves, while those in the imaginary part are represented by the corresponding markers.

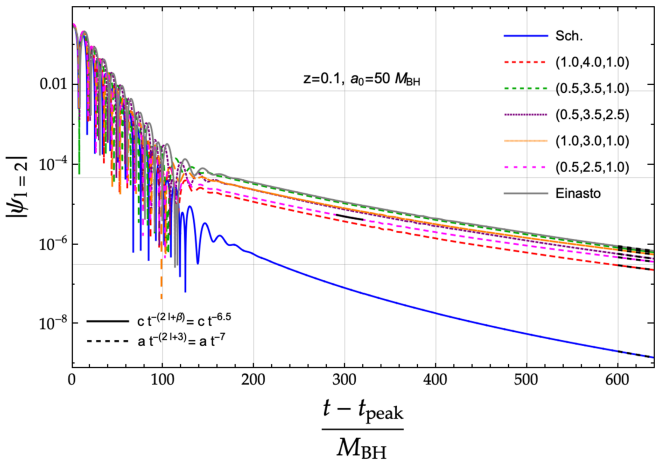


FIG. 12. Evolution of the Gaussian wave packet for different DM halo configurations. The solid blue curve corresponds to the Schwarzschild BH. The time coordinate is shifted such that the peaks of the ringdown coincide. To keep the time-domain evolution computationally tractable, we use representative values of $M_{\rm halo} \sim 5M_{\rm BH}$ and $a_0 \sim 50M_{\rm BH}$, without affecting the qualitative features of the ringdown and late-time tails. For the (1, 3, 1) and (0.5, 2.5, 1) halo profiles, the density is truncated at $r_t = 20.5a_0$. The solid black line shows the intermediate-tail scaling $t^{-(2l+\beta)} = t^{-6.5}$ for the (0.5, 2.5, 1) profile, while the dashed black line denotes the expected Price-law decay $t^{-(2l+3)} = t^{-7}$.

TABLE I. QNM frequencies computed from the time-domain signal in Fig. 12 and the corresponding values obtained from sixth-order WKB method for the $l = 2$ fundamental mode.

DM profiles	Prony fit	WKB (sixth order)
1.0, 4.0, 1.0	$0.3446328 - 0.0819501i$	$0.3446369 - 0.0819955\,i$
0.5, 3.5, 1.0	$0.3651418 - 0.0869178i$	$0.3651036 - 0.0868649i$
0.5, 3.5, 2.5	$0.3282496 - 0.0781977i$	$0.3282692 - 0.0781013i$
1.0, 3.0, 1.0	$0.3591402 - 0.0848168i$	$0.3591856 - 0.0854569i$
0.5, 2.5, 1.0	$0.3656644 - 0.0870637i$	$0.3656216 - 0.0869882i$
Einasto	$0.3163015 - 0.0752344i$	$0.3163734 - 0.0752711i$
Schwarzschild	$0.3736769 - 0.0889529i$	$0.3736194 - 0.0888910i$

$M_{\rm ADM} = M_{\rm BH} + M_{\rm halo}$), the standard asymptotic decay [$\psi(t) \propto t^{-(2l+3)}$] is eventually restored.

In Fig. 12, we plot the time profile for some representative DM distribution around the central spherically symmetric BH. It is useful to state the scales involved, since the parameters of Fig. 12 are compressed for numerical tractability. The intermediate tail comes from backscattering off the region in which the effective potential falls as $r^{-\beta}$, extending from the scale radius to the truncation radius. Its decay rate depends only on l and β, and the extent of the region only on the ratio r_t/a_0, so the compressed values of Fig. 12 entail no loss of generality. The wider truncation (relative to a_0) adopted there simply makes the intermediate scaling easier to identify. For $a_0 = 10^5 M_{\rm BH}$ with the truncation $r_t = 5a_0$ of Sec. II B, this region lies between $10^5 M_{\rm BH}$ and $5 \times 10^5 M_{\rm BH}$, that is, between 0.0048 and 0.24 pc for $M_{\rm BH} = 10^6 M_\odot$. The two decay rates are thus complementary: the intermediate exponent $2l + \beta$ measures the outer logarithmic slope, while the truncation radius fixes where the Price-law behavior is recovered.

We verify that at late time, perturbation decays follow Price's law. However, for (0.5, 2.5, 1) DM distribution with $\beta = 2.5$ an intermediate tail proportional to $t^{-2l-\beta} = t^{-6.5}$ is observed at intermediate times. The QNM frequencies and damping rate for the fundamental mode, obtained from Fig. 12 using the Prony method [119], match the corresponding sixth-order WKB results to a high accuracy, as shown in Table I.

VI. TIDAL LOVE NUMBERS

The analysis of the preceding sections showed that the entire ringdown spectrum responds to the DM environment through a single quantity, the redshift integral $\mathcal{I}$ of Eq. (50). Because the radial weight of $\mathcal{I}$ peaks near the inner cutoff, the QNM shift is most sensitive to the halo mass at *small* radii and hence to the inner logarithmic slope γ. In this section we compute a second, independent characterization of the same configuration, the static axial (magnetic-type) tidal Love number and show that it is governed by a differently weighted functional of the same halo mass distribution: an integral weighted toward large radii and controlled mostly by the compactness z, the outer logarithmic slope β, and the truncation radius r_t. The two quantities therefore probe complementary regions of the halo and respond to the shape parameters in opposite ways.

The (static) tidal Love number quantifies the conservative multipolar deformation induced in a compact object by an external static tidal field [72,73]. In vacuum general relativity in four spacetime dimensions, the static TLNs of a Schwarzschild BH vanish identically in both the polar (electric-type) and axial (magnetic-type) sectors [62,63]. However, a surrounding matter environment can induce a nonzero tidal response. Consequently, TLNs can act as a a powerful probe for surrounding environment. Here, we obtain the static axial TLNs of a Schwarzschild BH dressed with DM halo configurations of Sec. II analytically, to leading order in the halo compactness, and verify the result against numerical computations [95].

A. Static master equation

In the static limit, the axial sector isolates the tidal field. The $\theta\theta$ equation (28) reduces to a homogeneous first-order equation for h_1,

$$r(r-2m)h_1' + 2(m - 2\pi r^3 \bar{p})h_1 = 0, \tag{67}$$

while the $t\theta$ equation (32) loses its $\dot{h}_1$ terms and governs h_0 alone. The two sectors decouple. The nontrivial solution of Eq. (67), $h_1 \propto r/(r - 2M_{\rm BH})$ in the vacuum cavity, is not a tidal deformation. As h_1 cannot affect the response, we set $h_1 = 0$ with no loss of generality. This also removes the auxiliary vector from the problem: W appears only in the source of Eq. (30), so in the static limit the matter enters the perturbation equations through U alone.

Substituting the irrotational condition (34) into Eq. (32) and using the background relation (7), the matter terms combine as

$$\frac{8\pi\bar{\rho}(r-m)}{r-2m} - 16\pi(\bar{\rho} + \bar{p}_t) = -8\pi\bar{\rho} = -\frac{2m'}{r^2}, \tag{68}$$

so the static axial sector is governed by

$$\left(1 - \frac{2m}{r}\right)h_0'' - \frac{m'}{r}h_0' - \left[\frac{l(l+1)}{r^2} - \frac{4m}{r^3} - \frac{2m'}{r^2}\right]h_0 = 0. \tag{69}$$

Equation (69) coincides with the static axial equation of [95] for anisotropic fluids with vanishing radial pressure.

Two structural properties of Eq. (69) determine the physics of this section. First, the redshift function $f(r)$

has dropped out entirely—the static axial perturbation is sourced by the mass function $m(r)$ alone. The ringdown shift of Sec. IV B and the TLN thus probe two different radial weightings of the same halo mass distribution, and we quantify below how differently they respond to the shape parameters. Second, in the vacuum region $2M_{\rm BH} \le r \le 4M_{\rm BH}$, where $m = M_{\rm BH}$ and $m' = 0$, the solution of Eq. (69) regular at the horizon is

$$h_0^{(0)}(r) = Cr^{l+1}{}_2F_1(1-l,-l-2;-2l;2M_{\rm BH}/r). \quad (70)$$

For $l = 2$, this reduces to

$$h_0^{(0)}(r) \propto r^2(r-2M_{\rm BH}). \quad (71)$$

The large-r expansion of $h_0^{(0)}$ contains no admixture of the decaying solution, implying that the axial TLN of an isolated Schwarzschild BH vanishes. Equation (70) fixes the inner boundary data at the edge of the DM-free cavity without approximation.

B. Linear tidal response

In terms of the logarithmic derivative $y \equiv rh_0'/h_0$, Eq. (69) takes the Riccati form [63,120]

$$\left(1-\frac{2m}{r}\right)(ry' + y^2 - y) = m'y + l(l+1) - \frac{4m}{r} - 2m'. \quad (72)$$

The vacuum limit of Eq. (72) possesses two exact branches of solution, the growing branch [corresponding to Eq. (70)]

$$y_1 \approx l+1 \quad (73)$$

and a decaying branch with

$$y_2 \approx -l. \quad (74)$$

Horizon regularity selects Eq. (70) in the vacuum cavity, which is pure growing solution, the halo then mixes in a small amount of the decaying solution, and that admixture is the induced response. We therefore write

$$y(r) = y_1(r) + \delta y(r) \quad (75)$$

and linearize Eq. (72) in δy and in the halo, $m = M_{\rm BH} + m_h$, obtaining

$$r\delta y' + [2y_1(r) - 1]\delta y = \mathcal{S}[m_h, m_h'](r), \quad (76)$$

where the source $\mathcal{S}$ is $\mathcal{O}(z)$ and vanishes in vacuum. Two properties of Eq. (76) make the expansion well posed throughout the halo region, $4M_{\rm BH} \le r \le r_t$.

First, the homogeneous part of Eq. (76) is stable under outward integration. Its solution is $\delta y \propto r/[h_0^{(0)}]^2$, so the response is damped wherever the coefficient $2y_1 - 1$ is positive. This holds throughout the exterior. Evaluating the vacuum limit of Eq. (72) on the line $y = l+1$ forces

$$ry'|_{y=l+1} = \frac{2M_{\rm BH}(l-1)(l+2)}{r-2M_{\rm BH}} > 0, \quad (77)$$

so this line can be crossed only upward. The regular solution starts at $y \to +\infty$ at the horizon and hence remains above $l+1$ for all r, giving $2y_1 - 1 \ge 2l+1$. A halo-induced deviation therefore relaxes at least as fast as $r^{-(2l+1)}$ rather than growing. The growing branch is thus the attractor of the outward flow, and the expansion is stable.

Second, the expansion parameter is the halo compactness alone. The source in Eq. (76) is built from $m_h(r)/r$ and $m_h'(r)$, both $\mathcal{O}(z)$ throughout the halo, so $\delta y = \mathcal{O}(z)$.[3]

To carry out the linearization in the far zone $r \gg M_{\rm BH}$, where the halo resides, we introduce the integrating factor $[h_0^{(0)}(r)]^2/r$, whose leading form is r^{2l+1}. Thus, the first-order equation becomes

$$\frac{d}{dr}[r^{2l+1}\delta y] = (l-1)[m_h'(r)r^{2l} + 2(l+2)m_h(r)r^{2l-1}]. \quad (78)$$

At $l = 2$ the source collapses to the polynomial $8m_hr^3 + m_h'r^4$, so Eq. (78) is then exact to linear order in z on the *full* Schwarzschild background. For $l \ge 3$ the same construction holds to leading order, with fractional corrections $\mathcal{O}(M_{\rm BH}/a_0)$. Integrating from the cavity edge, where $\delta y = 0$,

$$\delta y(r_t) = \frac{(l-1)\mathcal{J}_l}{r_t^{2l+1}}, \quad (79)$$

$$\mathcal{J}_l \equiv \int_{4M_{\rm BH}}^{r_t} [m_h'r^{2l} + 2(l+2)m_hr^{2l-1}]dr = M_{\rm halo}r_t^{2l} + 4\int_{4M_{\rm BH}}^{r_t} m_hr^{2l-1}dr, \quad (80)$$

using $m_h(4M_{\rm BH}) = 0$ and $m_h(r_t) = M_{\rm halo}$ in the integration by parts.

Equation (79) is not yet the tidal response. For $r > r_t$ the spacetime is Schwarzschild with mass $M_{\rm ADM} = M_{\rm BH} + M_{\rm halo}$, so the applied tidal field is built on $M_{\rm ADM}$ rather than $M_{\rm BH}$, and the exterior solution

[3]Note that the response is small because the halo is dilute and extended ($z = M_{\rm halo}/a_0 \ll 1$), not because it is light. Also, since δy is measured relative to the exact vacuum solution and the cavity is vacuum, it vanishes identically there. The inner boundary condition is simply $\delta y(4M_{\rm BH}) = 0$.

reads $h_0 \propto h_0^{(0)}(r; M_{\rm ADM}) + \kappa_l r^{-l} + \cdots$, with κ_l the induced (decaying) amplitude, for which $\delta y^{\rm ext} = -(2l+1)\kappa_l r^{-(2l+1)}$. The part of $\delta y(r_t)$ set by the total enclosed mass $m_h(r_t) = M_{\rm halo}$, rather than by its radial distribution, merely renormalizes the mass of the applied field from $M_{\rm BH}$ to $M_{\rm ADM}$ and carries no information about the response, so it must be subtracted before the TLN is read off.[4] Matching y across r_t gives

$$\delta y(r_t) - \frac{(l-1)(l+2)}{l}\frac{M_{\rm halo}}{r_t} = -\frac{(2l+1)\kappa_l}{r_t^{2l+1}}, \quad (81)$$

in which the monopole term cancels through the identity $\frac{l+2}{l} M_{\rm halo} r_t^{2l} - \mathcal{J}_l = \frac{2}{l}\int m_h' r^{2l} dr$. The matching introduces two multiplicative prefactors because the interior perturbation is constructed about the Schwarzschild background with mass $M_{\rm BH}$, whereas the exterior solution is expressed in terms of the ADM mass $M_{\rm ADM} = M_{\rm BH} + M_{\rm halo}$. Each differs from unity by $O(M_{\rm halo}/r_t) \sim O(z)$. Since the induced tidal response is itself linear in the halo compactness, these prefactors modify the Love number only at $O(z^2)$ and are consistently neglected within our first-order perturbative treatment. The response then collapses to the compact result

$$\kappa_l = \frac{2(l-1)}{l(2l+1)} \int_{4M_{\rm BH}}^{r_t} m_h'(r) r^{2l} dr \quad (82)$$

$$= \frac{8\pi(l-1)}{l(2l+1)} \int_{4M_{\rm BH}}^{r_t} \bar{\rho}(r) r^{2l+2} dr, \quad (83)$$

which has no residual dependence on $M_{\rm BH}$. For the dominant quadrupole $l = 2$ this reduces to

$$\kappa_2 = \frac{1}{5}\int_{4M_{\rm BH}}^{r_t} m_h'(r) r^4 dr = \frac{4\pi}{5}\int_{4M_{\rm BH}}^{r_t} \bar{\rho}(r) r^6 dr, \quad (84)$$

which is exact at linear order in the halo mass on the full Schwarzschild background, the exact source cancellation of Eq. (78) being provably unique to $l = 2$. Equation (83) vanishes identically for $l = 1$, consistent with the fact that the static axial dipole represents a shift of angular momentum rather than an induced tidal response.[5] The induced magnetic-type multipole of each mass element grows as r^{2l}, so the axial tidal response is dominated by the *outermost* matter in the halo, in contrast to the redshift integral $\mathcal{I}$, whose weight $(r - 2M_{\rm BH})^{-1}$ favors the innermost matter. Since $m_h' r^{2l} \propto r^{2l+2-\beta}$, the moment in Eq. (83) is dominated by its upper limit for every $\beta < 2l + 3$, and the axial TLN of an untruncated halo is ill defined. This is the position-space manifestation of the logarithmic obstruction to the tidal matching identified in Ref. [95] for density profiles lacking compact support, and it makes a finite truncation radius r_t mandatory rather than optional. We fix r_t from the halo's own mass distribution. For a convergent profile ($\beta > 3$) the total halo mass is finite, and we identify r_t with the radius R_{99} enclosing 99% of it,

$$\int_{4M_{\rm BH}}^{R_{99}} m_h'(r) dr = 0.99 M_{\rm halo} \quad (\beta > 3). \quad (85)$$

For a divergent profile ($\beta \leq 3$, such as the NFW profile) the total mass grows without bound, R_{99} is undefined, and we adopt the fixed truncation $r_t = 5a_0$ used in Sec. II B. Both integrals implicit in Eq. (85) scale linearly with the density amplitude, so R_{99} is a functional of the profile shape alone, independent of $M_{\rm halo}$ and hence of the compactness z. Figure 13 shows R_{99} across the (γ, β) plane for three values of α: it grows as either logarithmic slope flattens, since matter is then distributed to larger radii, and shrinks as the profile steepens. Figure 14 shows the complementary dependence on a_0. For steep outer logarithmic slopes R_{99}/a_0 is nearly constant, however, as β approaches 3, it acquires a pronounced a_0 dependence, controlled by the fixed inner cutoff $4M_{\rm BH}$ relative to the scale radius. We render the induced multipole dimensionless following the relativistic convention of [62,95], normalizing by the total mass $M_{\rm ADM} = M_{\rm BH} + M_{\rm halo}$,

$$k_l^B \equiv -\frac{l+2}{l-1}\frac{\kappa_l}{M_{\rm ADM}^{2l+1}}, \qquad k_2^B = -\frac{4\kappa_2}{M_{\rm ADM}^5}, \quad (86)$$

which coincides with the definition of Refs. [72,94,95]. Since $\kappa_l > 0$, the matter-induced axial Love number is negative.

A word of caution about the magnitude of k_l^B is in order. The normalization by $M_{\rm ADM}^{2l+1}$ follows the standard relativistic convention, but for a BH dressed by an extended halo it carries the geometric factor $(r_t/M_{\rm ADM})^{2l+1}$. Here r_t exceeds $M_{\rm ADM}$ by several orders of magnitude, whereas for a self-gravitating body such as a neutron star the same ratio is only a few, and this difference accounts entirely for the very large values of $|k_2^B|$ reported below. They should not be read as indicating an unusually soft or easily deformed object: the physical response κ_2 is entirely ordinary and, as shown below, strictly linear in the halo mass.

[4] Consider a spherical shell of mass added around the BH. The shell shifts $M_{\rm BH} \to M_{\rm ADM}$ but, by spherical symmetry, induces no quadrupolar or higher deformation. The tidal response is therefore sourced not by the total halo mass but by its radial arrangement, through $\int m_h' r^{2l} dr$. The monopole piece is the difference of the two growing branches, $y_1(r; M_{\rm ADM}) - y_1(r; M_{\rm BH}) \to \frac{(l-1)(l+2)}{l}\frac{M_{\rm halo}}{r}$ at large r (equal to $2M_{\rm halo}/r$ for $l = 2$), which removes the $M_{\rm halo} r_t^{2l}$ term of $\mathcal{J}_l$ upon integration by parts.

[5] It is independently confirmed by a variation-of-parameters computation [121] (see [122] for details).

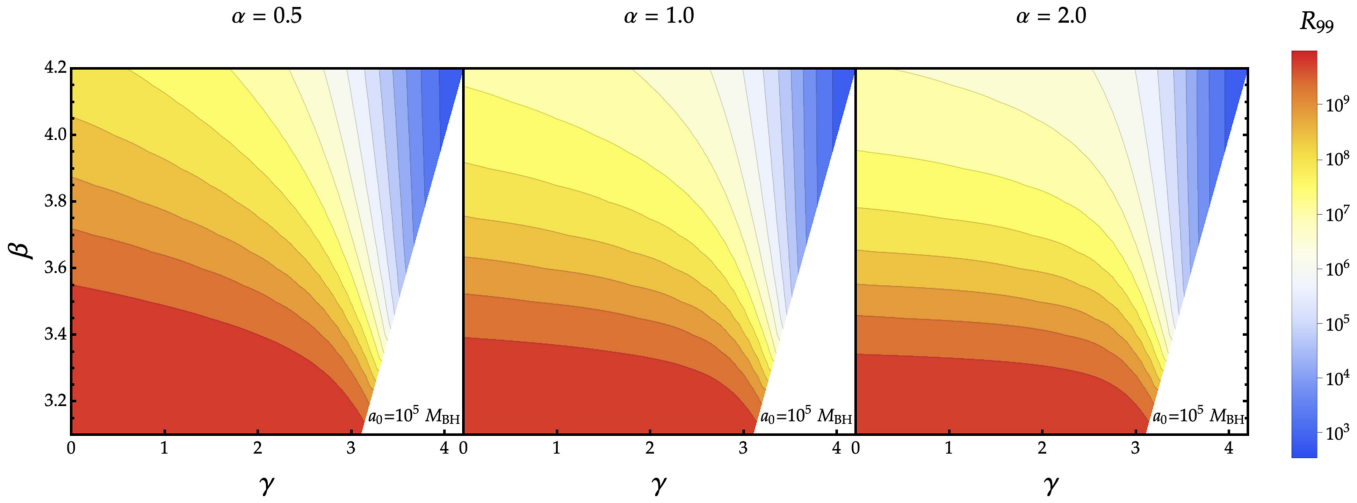


FIG. 13. The 99% mass radius R_{99} over the (γ, β) plane, at fixed $a_0 = 10^5 M_{\rm BH}$, for $\alpha = 0.5$, 1, 2. The white wedge is the unphysical region $\gamma \geq \beta$. R_{99} is largest for shallow profiles (small $\gamma, \beta \to 3^+$) and smallest for steep ones, spanning several decades across the shape parameters.

In the single-power-law limit, $\gamma \to \beta^-$ Eq. (83) evaluates in closed form,

$$\kappa_l = \frac{2(l-1)}{l(2l+1)} \frac{M_{\rm halo} \int_{4M_{\rm BH}}^{r_t} r^{2l+1-\beta}(r-4M_{\rm BH})dr}{\int_{4M_{\rm BH}}^{r_t} r^{1-\beta}(r-4M_{\rm BH})dr}$$
$$= \frac{2(l-1)}{l(2l+1)} \frac{M_{\rm halo}(2-\beta)(3-\beta)}{(2l+2-\beta)(2l+3-\beta)} \frac{(2l+2-\beta)r_t^{2l+3-\beta} - (2l+3-\beta)4M_{\rm BH} r_t^{2l+2-\beta} + (4M_{\rm BH})^{2l+3-\beta}}{(2-\beta)r_t^{3-\beta} - (3-\beta)4M_{\rm BH} r_t^{2-\beta} + (4M_{\rm BH})^{3-\beta}}, \quad (87)$$

depending on the halo only through $M_{\rm halo}$ and r_t. The scale radius a_0 drops out entirely, as it must: a pure power law fixes only the combination $\bar{\rho}_0 a_0^\beta$. Equation (87) further solidifies the choice of $M_{\rm ADM}$ as the normalizing length scale and provides an analytic anchor for the shape trends discussed below.

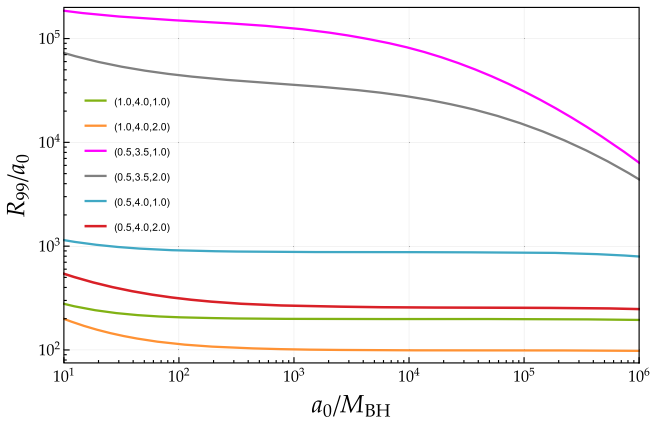


FIG. 14. The ratio R_{99}/a_0 as a function of a_0 for representative convergent profiles. For $\beta = 4$ the ratio is nearly independent of a_0, while for $\beta = 3.5$ it varies substantially, reflecting the growing influence of the fixed inner cutoff $4M_{\rm BH}$ as the outer logarithmic slope approaches the divergent value $\beta = 3$.

C. Dependence on compactness and halo parameters

At fixed shape and scale radius, the truncation radius R_{99} (or $5a_0$) is fixed, so the response is strictly linear in the halo mass, $\kappa_l \propto M_{\rm halo} \propto z$, as shown in the upper panel of Fig. 15. This linear growth does not contradict the familiar decrease of tidal Love numbers with increasing compactness for self-gravitating bodies. Since the Schwarzschild BH has a vanishing axial TLN, the response originates entirely from the surrounding halo, and z measures the amount of responding matter rather than the compactness of a fixed body. The dimensionless quantity k_2^B exhibits the opposite trend because its normalization depends on the total gravitating mass. Since

$$k_2^B \propto \frac{M_{\rm halo}}{(M_{\rm BH} + M_{\rm halo})^5}, \quad (88)$$

it decreases monotonically with z over the astrophysically relevant regime $M_{\rm halo} \gtrsim M_{\rm BH}$, as shown in the lower panel of Fig. 15. Unlike the physical response κ_2, this behavior is entirely a consequence of the conventional normalization

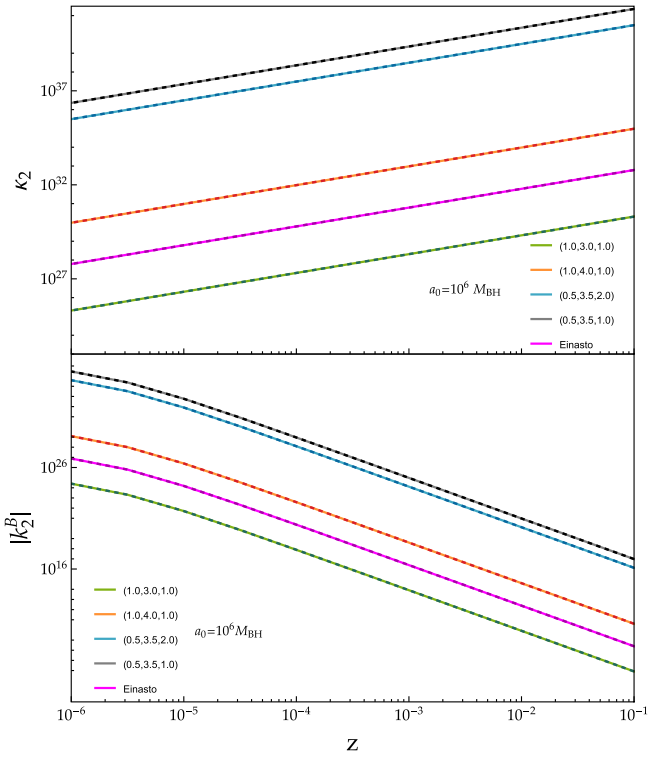


FIG. 15. The dimensionful response κ_2 (top) and the dimensionless Love number $|k_2^B|$ (bottom) as functions of compactness z, at $a_0 = 10^6 M_{\rm BH}$, for several halo profiles ($\beta > 3$ truncated at R_{99}, $\beta = 3$ at $5a_0$). Dashed curves are the numerical extraction, solid curves the analytic result, Eq. (83). κ_2 grows linearly with z, whereas $|k_2^B|$ decreases with z in accordance with Eq. (88).

by $M_{\rm ADM}^{2l+1}$ and is therefore consistent with the familiar trend that dimensionless TLNs decrease as the gravitating mass increases.

Figure 16 shows the variation of $|k_2^B|$ with the outer slope parameter β, in the two separate regimes of the outer slope. The split at $\beta = 3$ is where the halo mass ceases to converge, so the truncation radius is defined differently on either side. In the left panel $\beta < 3$ and $r_t = 5a_0$ is imposed externally. The extent is then common to all curves, and the panel isolates the effect of redistributing matter within a fixed radius. That effect is weak: $|k_2^B|$ falls by a factor of almost 1.9 across the β range. The weak dependence is specific to fixed truncation radius, increasing the fixed truncation radius only mildly increases the contrast ($\sim$10.95 for $r_t = 10^4 a_0$).

In the right panel the outer logarithmic slope is steep enough that the halo mass converges, so the truncation radius is set by the halo itself as R_{99}, the radius enclosing 99% of the mass. The tidal response is governed by this radius and grows approximately as its fourth power, as can be seen from Eq. (82) (see also [93]). Therefore, the steep fall of $|k_2^B|$ across the panel simply follows the shrinking of R_{99} as β increases in Fig. 13. The dependence is far from gentle. As β approaches 3 the outer density decays so slowly that an appreciable fraction of the mass sits at ever larger radii, and R_{99} must expand rapidly to contain 99% of it. Because R_{99} diverges as the halo mass stops converging at $\beta = 3$, the response rises sharply toward $\beta \to 3^+$. For $\beta > 3$ and fixed compactness as $M_{\rm halo}$ is increased the dimensionless response balances two competing effects of this extra mass, a suppression through the larger normalizing mass $M_{\rm ADM}$ and an enhancement through the larger truncation radius. For steep outer logarithmic slopes the truncation radius scales with a_0, so the enhancement wins. However, as $\beta \to 3^+$ the slow convergence of the mass causes the enhancement to disappear and only the suppression remains, enhancing the response of the lighter halo. The curves intersect where the two effects balance. This crossing is a consequence of using $r_t = R_{99}$. With a truncation radius tied to the halo's own scale the two curves remain parallel.

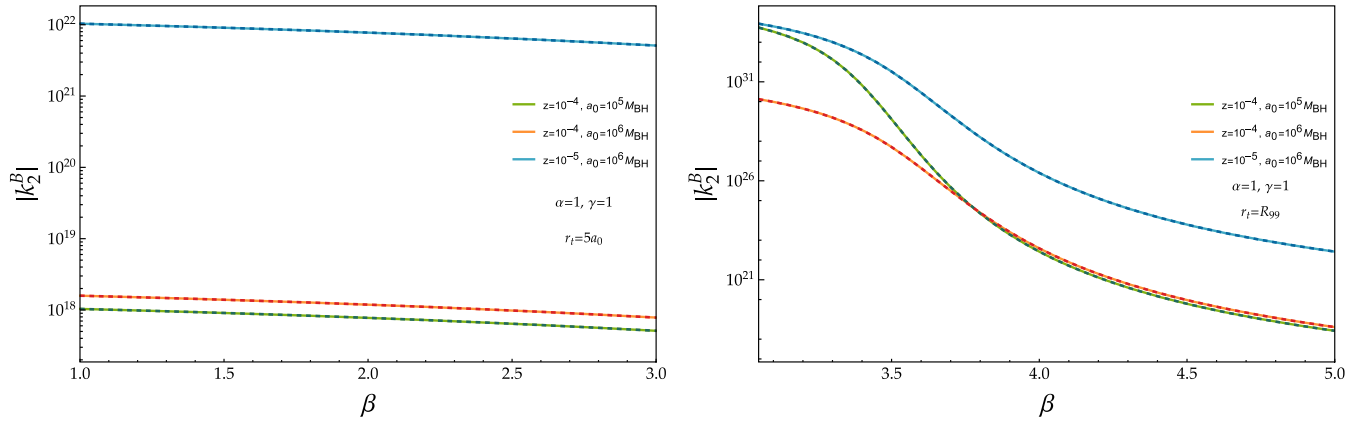


FIG. 16. Variation of $|k_2^B|$ with the outer logarithmic slope β, at fixed $\alpha = \gamma = 1$. The left panel shows the variation for the mass divergent profiles ($\beta < 3$) with fixed truncation radius at $r_t = 5a_0$. In contrast, the right panel plots the same with $\beta > 3$, and truncation radius $r_t = R_{99}$. Dashed curves, in both panels, represent numerically obtained values of $|k_2^B|$, whereas solid curves represent analytic results for different (z, a_0) combinations.

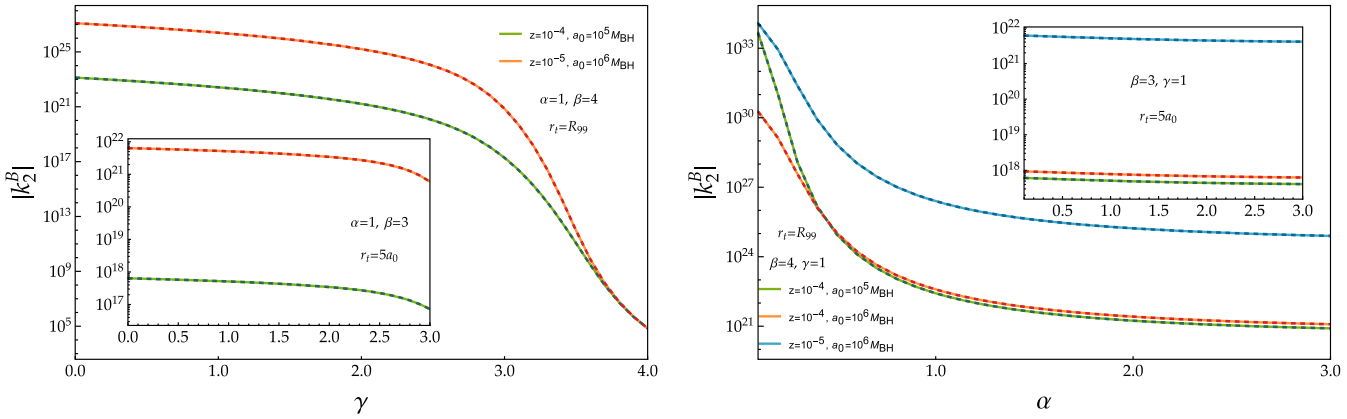


FIG. 17. Variation of $|k_2^B|$ with the inner logarithmic slope γ (left) and the transition sharpness α (right). In the left panel, $\alpha = 1$ and $\beta = 4$, while in the right panel $\beta = 4$ and $\gamma = 1$. In both panels, the truncation radius is chosen as $r_t = R_{99}$ for different combinations of a_0 and z. The insets show the corresponding results for $\beta = 3$ with a fixed truncation radius $r_t = 5a_0$. Dashed curves denote the numerical results, while solid curves show the analytic predictions.

Steepening the inner logarithmic slope γ transfers mass toward the inner region, so $|k_2^B|$ decreases with γ as well (right panel of Fig. 17). For $\beta > 3$ the decrease of $|k_2^B|$ with γ is further aided by the contraction of R_{99} (see Fig. 13). As γ approaches β the κ_2 become independent of a_0 [see Eq. (87)], this is coupled to the slow near independence of R_{99} on a_0 results in the converging value of $|k_2^B|$. However, for constant truncation radius $r_t = 5a_0$, the a_0 dependence persists even as γ approaches β.[6]

The parameter α controls how sharply the profile turns from its inner logarithmic slope γ to its outer logarithmic slope β near a_0, leaving both slope parameters unchanged. The right panel of Fig. 17 shows the variation of $|k_2^B|$ with α. In the main panel the response drops steeply with α. A broad transition (small α) keeps the density shallow well past a_0, so the halo is extended and R_{99} large, whereas a sharp transition confines the mass near a_0 and shrinks R_{99} (see Fig. 13). Since the response scales as R_{99}^4, this alone produces the decline, which steepens at small α and flattens once the transition is already sharp. The inset, with the truncation fixed at $5a_0$, shows that the effect of α on $|k_2^B|$ is small. Thus, the effect of α on $|k_2^B|$ in the main panel arises dominantly from the change in R_{99}.

The three curves share a common shape and differ only through the prefactor set by (z, a_0). The two curves at equal z cross once, near $\alpha \simeq 0.45$. A small α leaves the halo very extended, so R_{99} grows until it approaches the fixed outer radius used to normalize the total mass. The larger-a_0 halo reaches that limit first. It then loses the R_{99}^4 enhancement while keeping the penalty of its larger normalizing mass and so falls below the lighter curve. The crossing is therefore set by the fixed cutoff rather than by α itself. Unlike β, α does not change how fast the halo mass converges, so with a cutoff scaled to a_0 the curves would remain parallel.

VII. COMPLEMENTARITY OF AXIAL TLN AND QNM

The axial TLN exhibits the opposite dependence to the QNM shift $\delta\omega$, which increases with increasing inner halo density and steeper inner density profiles (Sec. IV B). This complementarity arises from the distinct radial weighting of the two observables: the axial TLN is primarily sensitive to the outer halo density, whereas the QNM shift is primarily sensitive to the inner halo density. The two observables therefore probe complementary regions of the same halo distribution.[7]

Figure 18 illustrates this complementarity on a representative (γ, β) slice at fixed (α, z, a_0). Contours of constant $|k_2^B|$ and $\delta\omega$ intersect over most of the parameter space and are colored by the complementary observable. The variation of the color along each contour demonstrates that models degenerate with respect to one observable generally predict distinct values of the other. Consequently, a joint measurement of $(|k_2^B|, \delta\omega)$ can substantially reduce the parameter degeneracies associated with either observable alone.

VIII. SUMMARY AND DISCUSSION

Astrophysical BHs are expected to reside in complex environments rather than in vacuum. From stellar-mass remnants embedded in gas-rich disks to supermassive BHs at galactic centers, the surrounding matter modifies the

[6]Note that halo distribution with larger mass and steeper inner logarithmic slope results in the appearance of additional light ring pairs (see Sec. II).

[7]An independent confirmation of this behavior for an alternative halo model will be presented in Ref. [122].

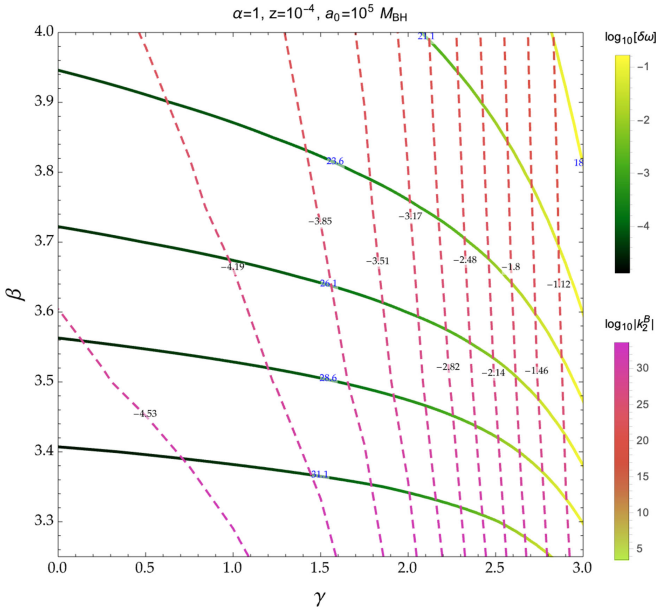


FIG. 18. Representative contour map illustrating the complementary dependence of the axial tidal Love number and the QNM redshift on the halo profile. The plot shows the (γ, β) plane for fixed $\alpha = 1$, $z = 10^{-4}$, and $a_0 = 10^5 M_{\rm BH}$. Solid curves are contours of constant $\log_{10}|k_2^B|$, while dashed curves are contours of constant $\log_{10}\delta\omega$. Each contour family is colored by the complementary observable: solid contours by $\log_{10}\delta\omega$ and dashed contours by $\log_{10}|k_2^B|$.

spacetime and can therefore influence GW observables [27–29,40,41,74]. As ringdown measurements become increasingly precise, understanding these environmental effects is essential both for interpreting observations and for using GWs as probes of the strong-field environment. The central question addressed in this work is whether GW observables are sensitive only to the total amount of surrounding matter or whether they also encode information about the *shape* of the DM distribution. This distinction is crucial because different halo profiles can produce similar shifts in a single observable, leading to degeneracies between the halo compactness, density profile, and possible deviations from the vacuum spacetime.

In this work we investigated the axial perturbations of a Schwarzschild BH surrounded by a generalized relativistic (α, β, γ) DM halo (Fig. 1) described within the Einstein-cluster formalism [54,55,94]. For this spacetime we derived the axial master equation, computed the quasinormal spectrum using sixth-order WKB method, and verified the results through time-domain evolution. We further derived the static axial tidal Love numbers analytically to leading order in the halo compactness and confirmed the analytic expressions by solving the full perturbation equations numerically.

Our analysis shows that the ringdown spectrum depends not only on the halo compactness but also on the detailed shape of the density profile. Increasing the halo compactness systematically redshifts both the oscillation frequency and the damping rate (Fig. 3), while the profile parameters produce additional corrections that become particularly significant for centrally concentrated halos. Among the shape parameters, the inner logarithmic slope γ has the strongest influence because the QNM redshift is governed by the halo redshift integral, whose kernel is concentrated near the inner cutoff. This behavior is reflected consistently in the light ring frequency, the principal Lyapunov exponent, the WKB spectrum, and the time-domain evolution. The time-domain analysis also reproduces the expected Price-law decay at late times together with the intermediate tail determined by the outer density profile for slowly decaying halos (Fig. 12).

The static tidal response behaves differently. The axial Love number vanishes identically for an isolated Schwarzschild BH. The surrounding halo renders it finite. To leading order, it is a high-order radial moment of the halo mass, weighted toward the outer halo. Its direct sensitivity is therefore to the outer logarithmic slope β and to the truncation radius, not to the inner cusp (Figs. 16 and 17). At fixed compactness its magnitude scales as the fourth power of the truncation radius r_t. Crucially, for halos that result in a convergent integrated mass the radius R_{99} enclosing 99% of the halo mass, contracts as *either* logarithmic slope steepens (Fig. 13). The Love number therefore falls steeply with both β and γ. The inner logarithmic slope acts only indirectly, by fixing the extent of the responding matter, not through the moment itself. Both trends oppose that of the ringdown redshift. The opposite dependence of the tidal response and the ringdown shift on the halo parameters follows directly from the distinct radial kernels governing the two observables.

The principal result of this work is that the ringdown and the static tidal response probe complementary regions of the same matter distribution. The QNM shift is governed by the redshift integral, which receives its dominant contribution from the vicinity of the inner cutoff, whereas the tidal Love number depends on an outer radial moment that is dominated by the extended halo. Consequently, halo configurations that are nearly degenerate in the ringdown generally predict different tidal deformabilities, and vice versa (Fig. 18). More generally, our results demonstrate that environmental effects cannot be characterized solely by the total halo mass or compactness; different GW observables respond to different moments of the surrounding matter distribution. Interpreting environmental effects therefore requires multiple observables rather than a single ringdown measurement.

To assess the potential observational relevance of these effects, we compared the predicted QNM shifts with the representative precision inferred from GW250114 [114,115]. For halo compactness $z = 10^{-4}$, a range of centrally concentrated profiles produces

frequency shifts of the same order as the current observational precision, whereas for $z = 10^{-6}$ only the most concentrated halos remain potentially distinguishable (Figs. 9 and 10). This comparison is intended only as an indication of the size of the effect rather than as an observational constraint. The GW250114 analysis assumes a Kerr remnant formed in a stellar-mass binary, whereas the present calculations describe a nonrotating BH embedded in a static DM environment. A quantitative constraint will require waveform models that consistently incorporate environmental effects throughout the inspiral, merger, and ringdown.

The present analysis relies on several key assumptions. The tidal response computed here rests on a choice of closure for the axial fluid velocity. Imposing irrotationality, $\omega^\mu = 0$, fixes the velocity through Eq. (34) and gives a configuration with $\delta u_\mu = 0$, although the fluid itself moves. The perturbed auxiliary vector δw_μ, and with it the function $W(t, r)$, is not an independent choice: it follows from the conservation of the perturbed energy-momentum tensor, Eq. (35). In the static sector, since $h_1 = 0$, the closure affects only through the term $4f(r)U$ in Eq. (32). Since that term is linear in U, a different closure changes the induced multipole only by an overall factor in the departure from irrotationality and not suppressed by the halo compactness. The magnetic-type Love numbers of matter-dressed BHs therefore depend on the closure adopted (see, e.g., [72], where a comoving closure $\delta u^\mu = 0$ has been used to study the static axial TLNs of a Schwarzschild-Hernquist black hole). The radial weighting, on the other hand, remains unchanged, since the departure enters through the same moment of the halo density that determines the response [Eq. (83)] itself. The complementarity with the ringdown redshift is thus robust against the choice of closure, and only the overall normalization is convention dependent.

We note that neither of the two dominant mechanisms that could drive the closure away from irrotationality, namely, viscosity and frame dragging, operate here. Viscosity does not arise in the present model at all: the Einstein-cluster construction describes collisionless particles moving on geodesics, so there is no viscous stress to include, and a collisional environment such as baryonic gas would require a different matter model and with it a different closure. Frame dragging is already contained in the treatment, since h_0 is itself a dragging potential and Eq. (34) carries the fluid along with it at the rate for which δu_μ vanishes. Dragging by the background is a separate matter and requires BH spin, which the present static geometry does not have.

The truncation radius is treated as a parameter of the finite-halo model and provides the natural normalization scale for the tidal response, with its influence becoming increasingly important as $\beta \to 3$. We further restrict the halo parameter space to configurations that do not admit additional light rings, thereby preserving the single-barrier potential structure underlying the WKB calculation of the QNM spectrum. Correlations among the halo parameters $(\alpha, \beta, \gamma, z, r_t)$ may also introduce residual degeneracies in observational inference. Finally, we restrict attention to axial perturbations of a nonspinning BH embedded in an Einstein-cluster halo with vanishing radial pressure. Extending the present framework to the polar sector, rotating BHs, and more general phase-space descriptions of the surrounding matter would broaden its applicability.

Looking ahead, the most promising observational target is likely to be an extreme-mass-ratio inspiral around a massive BH embedded in a dense DM environment [100]. Such systems naturally carry both observables considered here: the tidal response is encoded in the inspiral phasing, while the halo-induced QNM redshift appears in the subsequent ringdown. A direct observational implementation of this complementarity requires extending the present analysis to finite-radius perturbers, which we leave for future work. Combined with independent probes such as galactic rotation curves, which constrain the halo on much larger scales, these complementary GW signatures offer a promising route toward reconstructing the DM distribution in the immediate vicinity of BHs.

ACKNOWLEDGMENTS

The authors thank Vitor Cardoso for useful suggestions and comments. The authors also thank Sovan Chakraborty for insightful discussions and for providing computational resources. A. C. thanks Nils Andersson, Sanved Kolekar, and Sumanta Chakraborty for valuable discussions. A. C. also thanks Rajes Ghosh and Chiranjeeb Singha for useful comments. The work of A. C. was partly supported by the National Postdoctoral Fellowship of the Anusandhan National Research Foundation (ANRF), Government of India (File No. PDF/2023/000550) at IIT Guwahati. A. C. is grateful to the Raman Research Institute, Bangalore, for the hospitality extended during the conference "Symphony of Spacetime" where part of this work was carried out. S. C. acknowledges support of MATRICS research grant awarded by Science and Engineering Research Board (SERB) and ANRF, Government of India through Grant No. MTR/2022/000318.

DATA AVAILABILITY

There are no publicly available research data or software supporting this manuscript. Requests for further information or data should be sent to the authors.

APPENDIX A: ANALYTIC BASIS FOR THE LIGHT RING RESULTS

We derive the results quoted in Sec. IV A and provide the analytic basis for the trends seen in Figs. 4–6.

1. Redshift function at the light ring

The DM density vanishes for $r \leq 4M_{\rm BH}$. The mass function therefore satisfies $m(r_c) = M_{\rm BH}$, $\bar{\rho}(r_c) = 0$, and $m'(r_c) = 0$ at the light ring $r_c = 3M_{\rm BH}$. The local geometry at r_c is identical to the Schwarzschild case. The halo affects only the global value of $f(r_c)$.

Integrating Eq. (6) outward from r_c and imposing asymptotic flatness gives

$$\ln f(r_c) = -\int_{r_c}^{\infty} \frac{2m(r)}{r[r-2m(r)]}\,dr. \tag{A1}$$

We write $m = M_{\rm BH} + m_h$ and use the relation

$$\frac{2m}{r(r-2m)} - \frac{2M_{\rm BH}}{r(r-2M_{\rm BH})} = \frac{2m_h}{(r-2m)(r-2M_{\rm BH})}. \tag{A2}$$

Subtracting the vacuum integral gives $f(r_c) = \frac{1}{3}e^{-\mathcal{I}}$, which is Eq. (48), where $\mathcal{I}$ is the halo integral defined in Eq. (50),

$$\mathcal{I} \equiv \int_{4M_{\rm BH}}^{\infty} \frac{2m_h(r)}{[r-2m(r)][r-2M_{\rm BH}]}\,dr. \tag{A3}$$

An exterior spacetime requires $r > 2m(r)$ [note that in the absence of light ring the matter region invokes a stricter condition $r > 3m(r)$] and $m_h \geq 0$, so the integrand is non-negative and $\mathcal{I} > 0$ for any nonvanishing halo. Equation (49) then follows from $\Omega_c = \sqrt{f(r_c)}/r_c$ with $r_c = 3M_{\rm BH}$.

2. Universal identity $\lambda_c = \Omega_c$

We now derive the identity quoted as Eq. (51). We define $V_l(r) = f(r)/r^2$ and $g(r) = f(r)(1-2m/r)$, so $dr_*/dr = g^{-1/2}$. Since $V_l'(r_c) = 0$,

$$\left.\frac{d^2V_l}{dr_*^2}\right|_{r_c} = g(r_c)V_l''(r_c). \tag{A4}$$

At $r_c = 3M_{\rm BH}$, using $m(r_c) = M_{\rm BH}$, $m'(r_c) = 0$, and $f(r_c) = \frac{1}{3}e^{-\mathcal{I}}$,

$$g(r_c) = f(r_c)\left(1 - \frac{2M_{\rm BH}}{r_c}\right) = \frac{f(r_c)}{3}. \tag{A5}$$

Differentiating $f'/f = 2m/[r(r-2m)]$ at r_c with $m = M_{\rm BH}$ and $m' = 0$ gives

$$\frac{f'(r_c)}{f(r_c)} = \frac{2}{3M_{\rm BH}}, \tag{A6}$$

$$\frac{f''(r_c)}{f(r_c)} = \left(\frac{f'}{f}\right)^2\Bigg|_{r_c} + \left.\frac{d}{dr}\frac{2M_{\rm BH}}{r(r-2M_{\rm BH})}\right|_{r_c} = -\frac{4}{9M_{\rm BH}^2}. \tag{A7}$$

The quotient rule for $V_l = f/r^2$ then gives

$$V_l''(r_c) = \frac{f(r_c)}{r_c^2}\left[-\frac{4}{9M_{\rm BH}^2} - \frac{8}{9M_{\rm BH}^2} + \frac{6}{9M_{\rm BH}^2}\right] = -\frac{2f(r_c)}{3r_c^2M_{\rm BH}^2} < 0, \tag{A8}$$

consistent with a potential maximum. Inserting into Eq. (46) gives

$$\lambda_c^2 = -\frac{1}{2}\frac{r_c^2}{f(r_c)}g(r_c)V_l''(r_c) = \frac{f(r_c)}{r_c^2} = \Omega_c^2. \tag{A9}$$

Hence $\lambda_c = \Omega_c$ exactly. The key point is that $f(r_c)$ cancels in λ_c^2/Ω_c^2. The local derivatives of f at r_c depend only on $m(r_c) = M_{\rm BH}$ and $m'(r_c) = 0$, which take their Schwarzschild values for any halo profile. The halo changes only the overall scale of $f(r_c)$ through $\mathcal{I}$, and both Ω_c and λ_c pick up the same factor $e^{-\mathcal{I}/2}$. This confirms Eqs. (51) and (52) of the main text.

Setting $M_{\rm halo} = 0$ gives $m_h = 0$ and hence $\mathcal{I} = 0$. All results reduce to their Schwarzschild counterparts,

$$\Omega_c^{\rm Sch} = \lambda_c^{\rm Sch} = \frac{1}{3\sqrt{3}M_{\rm BH}}, \qquad \omega_{ln}^{\rm Sch} = \frac{l - i\left(n+\frac{1}{2}\right)}{3\sqrt{3}M_{\rm BH}}, \tag{A10}$$

confirming internal consistency.

3. Profile dependence of the halo integral

We now make precise the mechanisms described qualitatively in Sec. IV A.

a. Inner logarithmic slope γ

Near the inner cutoff. Setting $s \equiv r - 4M_{\rm BH}$ and expanding the right-hand side of Eq. (5) for $s \ll M_{\rm BH}$,

$$4\pi r^{2-\gamma}\left(1 - \frac{4M_{\rm BH}}{r}\right) = 4\pi(4M_{\rm BH})^{1-\gamma}s + O(s^2/M_{\rm BH}). \tag{A11}$$

The constant term cancels, so m_h vanishes quadratically,

$$m_h(r) = 2\pi\bar{\rho}_0 a_0^{\gamma}(4M_{\rm BH})^{1-\gamma}(r-4M_{\rm BH})^2 + O[(r-4M_{\rm BH})^3], \tag{A12}$$

for any γ. The integrand of $\mathcal{I}$ therefore vanishes at the lower limit for all $\gamma \geq 0$, so $\mathcal{I}$ is finite.

Power-law regime $4M_{\rm BH} \ll r \ll a_0$. Here the cutoff and outer transition factors are both negligible. Direct integration of $\bar{\rho} \approx \bar{\rho}_0 (r/a_0)^{-\gamma}$ gives, for $\gamma \neq 3$,

$$m_h(r) \approx \frac{4\pi \bar{\rho}_0 a_0^{\gamma}}{3-\gamma} [r^{3-\gamma} - (4M_{\rm BH})^{3-\gamma}]. \tag{A13}$$

Both limits are finite. The sign of $3-\gamma$ sets the behavior. For $\gamma < 3$, the exponent $3-\gamma > 0$ and $m_h \sim r^{3-\gamma}$ grows from zero. The enclosed fraction

$$\frac{m_h(r)}{M_{\rm halo}} \sim \left(\frac{r}{a_0}\right)^{3-\gamma} \ll 1 (r \ll a_0) \tag{A14}$$

stays small throughout the inner region, so most of $M_{\rm halo}$ sits at large radii $r \sim a_0$. For $\gamma > 3$, the exponent $3-\gamma < 0$ and $r^{3-\gamma}$ decreases with r. Numerator and denominator of Appendix (A13) are both negative, but their ratio is positive and increases with r, giving

$$\frac{m_h(r)}{M_{\rm halo}} \approx 1 - \left(\frac{4M_{\rm BH}}{r}\right)^{\gamma-3} \quad (r \gg 4M_{\rm BH}). \tag{A15}$$

This rises rapidly to unity just beyond $4M_{\rm BH}$, so most of $M_{\rm halo}$ sits close to the inner cutoff. At $\gamma = 3$, Appendix (A13) is replaced by $m_h \approx 4\pi \bar{\rho}_0 a_0^3 \ln(r/4M_{\rm BH})$.

Effect on $\mathcal{I}$. As γ increases, the dominant radial contribution to $\mathcal{I}$ moves from $r \sim a_0$, where $m_h \sim M_{\rm halo}$ but $(r-2M_{\rm BH})^{-1}$ is small, toward $r \sim 10$–$100M_{\rm BH}$, where $m_h \sim M_{\rm halo}$ and $(r-2M_{\rm BH})^{-1}$ is large. This inward shift steadily amplifies $\mathcal{I}$ and hence $\delta\Omega_c$, which is why Fig. 4 shows such a strong and rapid growth with γ. For $\gamma > 3$, the integrand is $O(M_{\rm halo}/M_{\rm BH}^2)$ over a radial extent $\sim M_{\rm BH}$ near the cutoff, so $\mathcal{I} \sim M_{\rm halo}/M_{\rm BH}$. This is parametrically larger than the $\gamma < 3$ contribution when $a_0 \gg M_{\rm BH}$.

b. Outer logarithmic slope β

At fixed $M_{\rm halo}$ and a_0, a larger β steepens the outer density falloff and requires a larger normalization $\bar{\rho}_0$ to keep the same total mass. This raises $m_h(r)$ at all radii, increasing $\mathcal{I}$ and hence $\delta\Omega_c$, as seen in Fig. 5. The effect is comparable to or weaker than the γ dependence over most of the range shown in the figures, but for small γ or a small gap $\beta - \gamma$, the sensitivity to β can match or exceed that of γ. This is most apparent as $\beta \to \gamma^+$, where the profile approaches a single power law, concentrating mass further inward and amplifying $\mathcal{I}$. The constraint $\beta > \gamma$ links the two slope parameters throughout.

c. Transition parameter α

A smaller α gives a smoother transition near $r \sim a_0$ and keeps more mass at intermediate radii, modestly raising $\bar{\rho}_0$ and hence $m_h(r)$ in the inner region. For larger γ, where the integrand of $\mathcal{I}$ carries appreciable weight at intermediate r, this raises $\mathcal{I}$, so $\delta\Omega_c$ decreases with α, as seen in Fig. 6. For small γ ($\gamma \lesssim 1$), the dependence on α is not weak and can even reverse sign: $\mathcal{I}$ increases with α the opposite of the large-γ trend above, with a nonmonotonic crossover near $\gamma \approx 1$. In both cases the α dependence remains subdominant.

4. Compactness scaling and degeneracy

At fixed (α, β, γ), rescaling $M_{\rm halo} \to \lambda M_{\rm halo}$ at fixed a_0 maps $m_h(r) \to \lambda m_h(r)$ at every fixed r, turning the single number $\mathcal{I}$, defined for one fixed halo, into a function $\mathcal{I}(\lambda)$ that can be differentiated. This is a bookkeeping device rather than a new physical parameter: the actual halo always has $\lambda = 1$, and every result below is evaluated there.

The compactness $z = M_{\rm halo}/a_0$ can equally be changed by holding $M_{\rm halo}$ fixed and varying a_0 instead, and the two routes are not interchangeable in general. For $4M_{\rm BH} \ll r \ll a_0$, where $m_h(r)/M_{\rm halo} \sim (r/a_0)^{3-\gamma}$ (Appendix A 3 a), sending $a_0 \to a_0/\mu$ at fixed $M_{\rm halo}$ multiplies z by μ, exactly as $\lambda \to \mu$ would, but it rescales $m_h(r)$ at fixed r by $\mu^{3-\gamma}$ rather than by μ, since μ enters inside the profile's argument r/a_0 rather than as an overall amplitude. The two routes therefore agree only where this distinction does not yet matter: in the linear regime established below, both give the same leading coefficient $C(\alpha, \beta, \gamma)$, because the dominant radial contribution to $\mathcal{I}$ sits at $r \ll a_0$ regardless of route, where the $\mu^{3-\gamma}$ versus μ^1 difference is a subleading correction. The two routes diverge once $\mathcal{I}$ is no longer small, as the saturation analysis of Appendix B 5 shows explicitly, where holding a_0 fixed and varying $M_{\rm halo}$ leads to a saturation value that depends on $M_{\rm halo}$, while holding $M_{\rm halo}$ fixed and varying a_0 does not change the saturation value at all. With this scope in mind, sweeping λ gives

$$\mathcal{I}(\lambda z) = \int_{4M_{\rm BH}}^{\infty} \frac{2\lambda m_h(r)}{[r - 2M_{\rm BH} - 2\lambda m_h(r)](r - 2M_{\rm BH})} dr. \tag{A16}$$

This is a monotonically increasing function of λ. Differentiating under the integral gives

$$\frac{d\mathcal{I}}{d\lambda} = \int_{4M_{\rm BH}}^{\infty} \frac{2m_h(r)}{[r - 2M_{\rm BH} - 2\lambda m_h(r)]^2} dr > 0. \tag{A17}$$

The integrand is non-negative because $m_h \geq 0$ and $r > 2M_{\rm BH} + 2\lambda m_h$ in the exterior. A second derivative gives $d^2\mathcal{I}/d\lambda^2 > 0$, so $\mathcal{I}$ is convex in λ. The integrand $8m_h^2/[r - 2m(r)]^3$ is manifestly positive in the exterior, where $r > 3m(r)$ (Appendix A 1) ensures $r - 2m(r) > m(r) > 0$. As λ grows, the denominator $r - 2M_{\rm BH} - 2\lambda m_h$ shrinks and the integrand grows faster than linear.

The eikonal shift $\delta\Omega_c = 1 - e^{-\mathcal{I}/2}$ is monotonically increasing in λ (since $\mathcal{I}' > 0$).[8]

a. Linear regime

The linear approximation $\mathcal{I} \approx Cz$ holds when the term $2\lambda m_h(r)$ in the denominator of Appendix (A16) stays small compared with $r - 2M_{\rm BH}$ at every radius where the integrand matters. The dominant radial scale, and so the condition for linearity, depends on γ.

For $\gamma \lesssim 2$, the integrand of $\mathcal{I}$ is dominated by $r \sim a_0$ (Appendix A 3 a), where $m_h(r) \sim M_{\rm halo}$ and $r - 2M_{\rm BH} \sim a_0$. The smallness condition then reads $2M_{\rm halo} \ll a_0$, that is $z \ll \frac{1}{2}$, which holds throughout the range $z \ll 1$ shown in the figures. The denominator reduces to $(r - 2M_{\rm BH})^2$, giving

$$\mathcal{I} \approx C(\alpha,\beta,\gamma)z, \qquad C(\alpha,\beta,\gamma) \equiv \int_{4M_{\rm BH}}^{\infty} \frac{2\hat{m}_h(r)a_0}{(r-2M_{\rm BH})^2}\,dr, \tag{A18}$$

where $\hat{m}_h(r) = m_h(r)/M_{\rm halo}$ is the normalized enclosed mass, independent of z. Hence $\delta\Omega_c \approx \frac{1}{2}C(\alpha,\beta,\gamma)z$ for $\gamma \lesssim 2$.

As γ approaches 3, the radial scale that dominates the integrand of $\mathcal{I}$ moves inward gradually rather than switching abruptly at $\gamma = 3$. Numerically, the fraction of $\mathcal{I}$ coming from $r < 100M_{\rm BH}$ rises from below 1% at $\gamma = 1$ to about 70% at $\gamma = 2.9$, for $a_0 = 10^5 M_{\rm BH}$, and this fraction barely changes with z over the range shown. Equation (A18) therefore becomes a progressively cruder approximation for $2 \lesssim \gamma < 3$, even though $\mathcal{I}$ stays approximately linear in z across this range. The dominant radial scale shifts, but at fixed γ the integral remains linear in λ to leading order, since the inner contribution is governed by Appendix (B4) of Appendix B 1, which is itself linear in $M_{\rm halo}$ wherever its validity condition holds.

For $\gamma \geq 3$, the integrand of $\mathcal{I}$ is dominated by $r \sim \text{few}M_{\rm BH}$, where $m_h(r) \sim M_{\rm halo}$ and $r - 2M_{\rm BH} \sim M_{\rm BH}$. The smallness condition then becomes $2M_{\rm halo} \ll M_{\rm BH}$, that is $z \ll M_{\rm BH}/a_0$. For the astrophysically relevant case $a_0 \gg M_{\rm BH}$, this threshold sits far below the $z \ll 1$ range of the figures. For $a_0 = 10^5 M_{\rm BH}$ one needs $z \ll 10^{-5}$. So for $\gamma \geq 3$, $\mathcal{I}$ is already in the nonlinear, convex regime through most of the plotted compactness range and grows faster than linear in z. The same threshold, generalized to $z \ll (M_{\rm BH}/a_0)^{\gamma-2}$, governs the onset of nonlinearity already for $2 < \gamma < 3$ (Appendix B 1).

The two compactnesses $z = (10^{-6}, 10^{-4})$ in the right panels of Figs. 4–6 are obtained by holding $M_{\rm halo}$ fixed and varying a_0. Under this route, z still increases by the same factor of 10^2 between the two curves, but $m_h(r)$ at fixed r no longer rescales by that same factor: writing $a_0 \to a_0/\mu$ at fixed $M_{\rm halo}$ multiplies z by μ while rescaling $m_h(r)$ at fixed r by $\mu^{3-\gamma}$ in the power-law regime (Appendix A 3 a), not by μ^1. For $\gamma \lesssim 2$, where the linear regime holds most robustly and $3 - \gamma$ is not too small, $\delta\Omega_c$ still grows by close to the full 10^2 between the two curves, since the dominant radial contribution to $\mathcal{I}$ sits at $r \ll a_0$ for both choices of a_0, where the precise value of a_0 matters little to the integral beyond setting its overall normalization. As γ rises toward 3, however, $3 - \gamma \to 0$ and the $\mu^{3-\gamma}$ rescaling of $m_h(r)$ weakens sharply, so the separation between the two compactness curves *shrinks*. This is opposite to what naive linear-in-z scaling would suggest and the opposite of what would be seen under the $M_{\rm halo}$ route instead, where the separation stays close to 10^2 at every γ because $m_h(r)$ there rescales by the full factor μ regardless of γ (Appendix A 4). This is consistent with the saturation mechanism of Appendix B 5: as $\gamma \to \beta^-$, $\mathcal{I}$ becomes insensitive to a_0 altogether, and the shrinking separation seen here is the finite-γ precursor of that same effect. This matches the behavior visible directly in the eikonal panels of Fig. 4, where the two compactness curves converge as $\gamma \to 3$; the corresponding contrast with the $M_{\rm halo}$ route, where the separation does not shrink, is shown for the noneikonal quantity $\delta\omega$ in Fig. 7 and discussed in Appendix B 5.

b. Degeneracy

$\delta\Omega_c = 1 - e^{-\mathcal{I}/2}$ depends on (α,β,γ,z) only through the single number $\mathcal{I}$. Any combination with $\beta > \gamma$ that gives the same $\mathcal{I}$ gives the same light ring shift. For $\gamma > 3$, where $\mathcal{I} \sim M_{\rm halo}/M_{\rm BH}$, a given shift is reached at smaller z than for $\gamma < 3$, so a steep inner cusp at low compactness can mimic a shallower cusp at higher compactness. This produces the degeneracy surfaces in Fig. 4. The boundary $\beta > \gamma$ marks the edge of the physically allowed region. Breaking this degeneracy needs either subleading corrections to the uniform potential scaling or independent astrophysical priors on the halo profile.

APPENDIX B: ANALYTIC BASIS FOR THE NONEIKONAL QNM RESULTS

We derive the results and trends described in Sec. IV B and provide the analytic basis for the observations in Figs. 3–7.

1. Potential scaling and exact frequency relation

The Regge-Wheeler potential governing axial perturbations, Eq. (40), reads

$$V(r) = f(r)\left[\frac{l(l+1)}{r^2} - \frac{6m(r)}{r^3} + \frac{m'(r)}{r^2}\right]. \tag{B1}$$

[8]It is interesting to note that, for most of the DM distributions studied in the present work, we observe $\delta\Omega_c$ to be a concave function of $\mathcal{I}$, implying $(\mathcal{I}')^2 > 2\mathcal{I}''$.

TABLE II. Comparison of the angular frequency and the principal Lyapunov exponent at the light ring with the fundamental QNM frequencies obtained using sixth order WKB method for different multipoles for different halo configurations with compactness $z = 10^{-4}$ and scale radius $a_0 = 10^5$. For the Einasto profile $r_e = a_0$. The Schwarzshild values are also shown for reference.

DM profile	l	From light ring frequency	From WKB-6
0.5, 3.5, 1	2	$0.3848872 - 0.0962218i$	$0.3736068 - 0.0888880i$
	3	$0.5773308 - 0.0962218i$	$0.5994232 - 0.0926994i$
	10	$1.9244360 - 0.0962218i$	$1.9967205 - 0.0958606i$
0.5, 3.5, 2.5	2	$0.3805829 - 0.0951457i$	$0.3694286 - 0.0878939i$
	3	$0.5708744 - 0.0951457i$	$0.5927197 - 0.0916627i$
	10	$1.9029146 - 0.0951457i$	$1.9743907 - 0.0947886i$
1, 3, 1	2	$0.3848667 - 0.0962167i$	$0.3735869 - 0.0888832i$
	3	$0.5773001 - 0.0962167i$	$0.5993913 - 0.0926945i$
	10	$1.9243336 - 0.0962167i$	$1.9966142 - 0.0958555i$
1, 3, 2.5	2	$0.3819387 - 0.0954847i$	$0.3707447 - 0.0882070i$
	3	$0.5729081 - 0.0954847i$	$0.5948312 - 0.0919893i$
	10	$1.9096936 - 0.0954847i$	$1.9814243 - 0.0951263i$
1, 4, 1	2	$0.3848617 - 0.0962154i$	$0.3735820 - 0.0888821i$
	3	$0.5772926 - 0.0962154i$	$0.5993834 - 0.0926932i$
	10	$1.9243085 - 0.0962154i$	$1.9965882 - 0.0958543i$
1, 4, 2.5	2	$0.3803444 - 0.0950861i$	$0.3691971 - 0.0878388i$
	3	$0.5705166 - 0.0950861i$	$0.5923482 - 0.0916053i$
	10	$1.9017221 - 0.0950861i$	$1.9731534 - 0.0947292i$
Einasto	2	$0.3847691 - 0.0961923i$	$0.3734921 - 0.0888607i$
	3	$0.5771536 - 0.0961923i$	$0.5992392 - 0.0926710i$
	10	$1.9238454 - 0.0961923i$	$1.9961077 - 0.0958312i$
Schwarzschild	2	$0.3849002 - 0.0962250i$	$0.3736194 - 0.0888910i$
	3	$0.5773503 - 0.0962250i$	$0.5994434 - 0.0927025i$
	10	$1.9245009 - 0.0962250i$	$1.9967878 - 0.0958639i$

This potential is defined on the full domain $r \in [2M_{\rm BH}, \infty)$, with or without the halo. Its functional form changes at $r = 4M_{\rm BH}$ because the halo density $\bar{\rho}(r)$, and hence $m(r)$ and $f(r)$, is defined piecewise. $\bar{\rho}(r) = 0$ for $r \le 4M_{\rm BH}$, the assumed DM-free cavity, and $\bar{\rho}(r) > 0$ for $r > 4M_{\rm BH}$. We treat $V_{\rm DM}(r)$ on these two subdomains in turn and ask in each case how closely it tracks $e^{-\mathcal{I}} V_{\rm Sch}$.

a. Subdomain $r \le 4M_{\rm BH}$

Here $\bar{\rho} = 0$ and $m_h = 0$, so $m = M_{\rm BH}$ and $m' = 0$. Both $f_{\rm DM}$ and $f_{\rm Sch}$ obey the same first-order ordinary differential equation, Eq. (6),

$$\frac{f'}{f} = \frac{2M_{\rm BH}}{r(r - 2M_{\rm BH})}, \tag{B2}$$

and so differ only by a multiplicative constant fixed by their boundary conditions at large r. From Appendix A this constant is $e^{-\mathcal{I}}$, where $\mathcal{I}$ is the halo integral of Eq. (50), a fixed number rather than a function of r. Therefore

$$V_{\rm DM}(r) = e^{-\mathcal{I}} V_{\rm Sch}(r) \quad (r \le 4M_{\rm BH}) \tag{B3}$$

exactly. $V_{\rm DM}$ is simply $V_{\rm Sch}$ rescaled by the constant $e^{-\mathcal{I}}$, so it has the same shape and the same extrema, lowered uniformly in amplitude. A positive rescaling does not move an extremum, so any local maximum of $e^{-\mathcal{I}} V_{\rm Sch}(r)$ on this subdomain sits at the same r as the corresponding extremum of $V_{\rm Sch}$. We show below that for $l \ge 2$ this extremum, the global potential maximum, falls at $r_{\rm max} < 4M_{\rm BH}$, inside this subdomain. Whether it is also the global maximum of $V_{\rm DM}(r)$ over the full domain depends on the other subdomain, treated next.

b. Subdomain $r > 4M_{\rm BH}$

Here $m_h(r) > 0$ and $\bar{\rho}(r) > 0$, so Appendix (B3) no longer holds exactly. Even so, $V_{\rm DM}(r) \approx e^{-\mathcal{I}} V_{\rm Sch}(r)$ remains an excellent approximation, for reasons that depend on γ.

The size of $m_h(r)$ at $r \sim \text{few} M_{\rm BH}$, well inside a_0, refines the simple split between $\gamma < 3$ and $\gamma > 3$. From the enclosed-mass fraction of Appendix A 3 a, $m_h(r)/M_{\rm halo} \sim (r/a_0)^{3-\gamma}$ for $4M_{\rm BH} \ll r \ll a_0$ and $\gamma < 3$. Writing $M_{\rm halo}/M_{\rm BH} = z a_0/M_{\rm BH}$, the enclosed mass at $r \sim cM_{\rm BH}$ with $c = O(1)$ scales as

$$\frac{m_h(cM_{\rm BH})}{M_{\rm BH}} \sim z c^{3-\gamma} \left(\frac{M_{\rm BH}}{a_0}\right)^{2-\gamma}. \tag{B4}$$

For $\gamma \le 2$ the exponent $2 - \gamma \ge 0$, so $(M_{\rm BH}/a_0)^{2-\gamma} \le 1$, and Appendix (B4) holds trivially. $m_h(r) \ll M_{\rm BH}$ for any $z \ll 1$. For $2 < \gamma < 3$ the exponent flips sign, $(M_{\rm BH}/a_0)^{2-\gamma} = (a_0/M_{\rm BH})^{\gamma-2} \gg 1$, and the bound needs the stronger condition

$$z \ll \left(\frac{M_{\rm BH}}{a_0}\right)^{\gamma-2} \quad (2 < \gamma < 3), \tag{B5}$$

which tightens as $\gamma \to 3^-$ and in that limit matches onto the threshold $z \ll M_{\rm BH}/a_0$ derived below for $\gamma > 3$. For $a_0 = 10^5 M_{\rm BH}$, Appendix (B5) requires $z \ll 3 \times 10^{-5}$ at $\gamma = 2.9$, so $m_h(r) \ll M_{\rm BH}$ can fail at moderate compactness even when $\gamma < 3$. Where Appendix (B5) holds, the ratio $V_{\rm DM}/V_{\rm Sch} \approx e^{-\mathcal{I}}$ is preserved through the inner region, up to corrections of order $m_h(r)/M_{\rm BH} \ll 1$. Near $r \sim a_0$, where $m_h(r) \sim M_{\rm halo}$, this approximation breaks down regardless of γ. There, $V(r) \sim l(l+1)/r^2 \sim l(l+1)/a_0^2$ is negligible against ω^2, so the contribution to the QNM condition is suppressed by $(M_{\rm BH}/a_0)^2 \ll 1$ either way. This is a magnitude bound, not the exact value of V: the other two terms in Appendix (B1) stay subdominant to the centrifugal term, since $-6m(r)/r^3$ is suppressed by a factor $\sim M_{\rm BH}/r$, and $m'(r)/r^2$ carries an overall factor $\sim z/l(l+1) \ll 1$ from the small compactness. Both corrections stay below the leading term throughout $r > 4M_{\rm BH}$.

For $\gamma \ge 3$ [and for γ near 3 at the compactnesses used in the figures, where Appendix (B5) fails], $m_h(r) \sim M_{\rm BH}$

already at $r \sim \text{few} M_{\rm BH}$, so the $O(m_h/M_{\rm BH})$ correction to $V_{\rm DM}$ is not small in the DM-occupied zone. Nevertheless, the potential barrier governing the $l \geq 2$ fundamental mode is concentrated at $r < 4M_{\rm BH}$ (shown below), where Appendix (B3) holds exactly. The modification to $V_{\rm DM}$ for $r > 4M_{\rm BH}$ enters only the classically allowed propagating region and contributes a only a small correction to the outgoing wave phase.

In either case, $V(r)$ at $r > 4M_{\rm BH}$ stays bounded by $\sim l(l+1)/r^2$, for the same reason given above, and this never reaches the value $V_{\rm max} = e^{-\mathcal{I}} V_{\rm Sch}(r_{\rm max})$ attained at $r_{\rm max} < 4M_{\rm BH}$ on the first subdomain. No competing maximum appears for $r > 4M_{\rm BH}$, so $r_{\rm max}$, computed below from the exact rescaling Appendix (B3), is the global maximum of $V_{\rm DM}(r)$, not merely a local one confined to $r \leq 4M_{\rm BH}$.

The uniform scaling $V_{\rm DM} \approx e^{-\mathcal{I}} V_{\rm Sch}$ therefore holds across the QNM-relevant region in both cases. To estimate the residual correction from $r > 4M_{\rm BH}$, we use the standard real-axis WKB heuristic of the numerical QNM literature [57,58], in which the potential barrier extends between the points where $V(r) = \omega_{\rm Re}^2$ on the real r-axis.[9] We quantify this correction below, after deriving the Schwarzschild potential maximum and its value at the cutoff.

The tortoise coordinate satisfies $dr_*/dr = [f(r) \times (1 - 2m/r)]^{-1/2}$. For $r \leq 4M_{\rm BH}$, using $m = M_{\rm BH}$ and $f_{\rm DM} = e^{-\mathcal{I}} f_{\rm Sch}$,

$$\frac{dr_*^{\rm DM}}{dr} = \frac{1}{\sqrt{e^{-\mathcal{I}} f_{\rm Sch}(r)(1 - 2M_{\rm BH}/r)}} = e^{\mathcal{I}/2} \frac{dr_*^{\rm Sch}}{dr}. \tag{B6}$$

Since $\mathcal{I}$ is a constant, integrating gives $r_*^{\rm DM} = e^{\mathcal{I}/2} r_*^{\rm Sch} + C$ with C a constant of integration, and no $d\mathcal{I}/dr_*$ term appears. Applying the chain rule $d/dr_*^{\rm DM} = e^{-\mathcal{I}/2} d/dr_*^{\rm Sch}$ to the DM Regge-Wheeler equation and using Appendix (B3) gives

$$e^{-\mathcal{I}} \frac{d^2\psi}{dr_*^{\rm Sch2}} + [\omega_{\rm DM}^2 - e^{-\mathcal{I}} V_{\rm Sch}]\psi = 0. \tag{B7}$$

Multiplying through by $e^{\mathcal{I}}$ gives

$$\frac{d^2\psi}{dr_*^{\rm Sch2}} + [e^{\mathcal{I}} \omega_{\rm DM}^2 - V_{\rm Sch}(r_*^{\rm Sch})]\psi = 0 \quad (r \leq 4M_{\rm BH}), \tag{B8}$$

the Schwarzschild Regge-Wheeler equation with ω replaced by $e^{\mathcal{I}/2}\omega_{\rm DM}$. At the horizon ($r_*^{\rm Sch} \to -\infty$), the ingoing boundary condition $\psi \sim e^{-i\omega_{\rm DM} r_*^{\rm DM}} = e^{-i\omega_{\rm DM} e^{\mathcal{I}/2} r_*^{\rm Sch}} \times$ phase matches the Schwarzschild form with $\omega_{\rm Sch} = e^{\mathcal{I}/2}\omega_{\rm DM}$. The integration constant C adds only an irrelevant overall phase. The QNM resonance condition then gives

$$\omega_{\rm DM} = e^{-\mathcal{I}/2}\omega_{\rm Sch}, \tag{B9}$$

and hence

$$\delta\omega_{\rm Re} = \delta\omega_{\rm Im} = 1 - e^{-\mathcal{I}/2} = \delta\Omega_c. \tag{B10}$$

The fractional redshifts of the real and imaginary parts of the QNM frequency match each other and the light ring shift $\delta\Omega_c$ for every multipole $l \geq 2$, every overtone, and every halo profile. This is why $\delta\omega_{\rm Re}$ and $\delta\omega_{\rm Im}$ overlap so closely in Fig. 6 and why both track the eikonal shifts there.

The derivation rests on Appendix (B3) holding through the region that sets the QNM eigenvalue, bounded within the real-axis heuristic by the points where $V(r) = \omega_{\rm Re}^2$. Setting $dV/dr = 0$ for the Schwarzschild potential with $V = (1 - 2M/r)[l(l+1)/r^2 - 6M/r^3]$ gives the quadratic $2Lr^2 - 6M(3+L)r + 48M^2 = 0$, where $L = l(l+1)$, whose outer root gives the potential maximum

$$r_{\rm max}(l) = \frac{3(3+L) + \sqrt{9(3+L)^2 - 96L}}{2L} M_{\rm BH},$$
$$r_{\rm max}(l) \xrightarrow{l\to\infty} 3M_{\rm BH}. \tag{B11}$$

For $l = 2$ ($L = 6$) this evaluates analytically to $r_{\rm max} = \frac{1}{4}(9 + \sqrt{17})M_{\rm BH} \approx 3.28M_{\rm BH}$, inside the DM-free zone. The potential at the inner cutoff evaluates analytically to

$$V(4M_{\rm BH}) = \frac{9}{64M_{\rm BH}^2} \quad (l = 2). \tag{B12}$$

V falls monotonically beyond $r_{\rm max}$, so the heuristic outer boundary satisfies $V(r_{\rm outer}) = \omega_{\rm Re}^2$, and $r_{\rm outer}$ falls outside $4M_{\rm BH}$ only if $\omega_{\rm Re}^2 < V(4M_{\rm BH})$. Numerically, $\omega_{\rm Re}^2 \approx 0.9929 V(4M_{\rm BH})$ for the $l = 2$, $n = 0$ mode, so $r_{\rm outer}$ sits just outside $4M_{\rm BH}$, with $r_{\rm outer} - 4M_{\rm BH} \approx [V(4M_{\rm BH}) - \omega_{\rm Re}^2]/|V'(4M_{\rm BH})| \approx 0.04M_{\rm BH}$. The WKB phase accumulated in the strip $[4M_{\rm BH}, r_{\rm outer}]$ is

[9] This is a leading-order approximation, valid when $|\omega_{\rm Im}| \ll \omega_{\rm Re}$. For $l = 2$, $n = 0$, $|\omega_{\rm Im}/\omega_{\rm Re}| \approx 0.24$, so it is indicative rather than exact. The rigorous treatment locates turning points as zeros of $Q_0(r) = \omega^2 - V(r)$ in the complex r-plane, as in the exact WKB formalism of Miyachi *et al.* [123]. For $r < 4M_{\rm BH}$, Q_0 inherits the meromorphic structure of the Schwarzschild problem exactly under $\omega \to e^{\mathcal{I}/2}\omega_{\rm DM}$, so an exact-WKB treatment of this region alone should be achievable in principle. For $r > 4M_{\rm BH}$, the profile factor $[1 + (r/a_0)^\alpha]^{(\gamma-\beta)/\alpha}$ has branch points in the complex plane for generic noninteger α, so $Q_0(r)$ is not meromorphic there and the Borel-summation machinery behind exact WKB treatment does not directly apply. A full treatment would also need $r = 4M_{\rm BH}$ as an interior matching point joining the WKB bases of the two regions, a connection problem not covered by the existing literature, which treats only the two asymptotic ends. We regard a full exact-WKB treatment of the generic (α, β, γ) profile as out of reach with current methods, though tractable for restricted cases such as integer α, and leave it for future work.

$$\phi_{\rm strip} \approx \frac{1}{f(4M_{\rm BH})}\sqrt{|V'(4M_{\rm BH})|}\frac{2}{3}(r_{\rm outer}-4M_{\rm BH})^{3/2}. \tag{B13}$$

The Schutz-Will quantization condition [58] requires the full barrier integral $\phi_{\rm total}$ to equal $(n+\frac{1}{2})\pi = \pi/2$ for the fundamental mode; a fractional shift $\phi_{\rm strip}/(\pi/2)$ in that integral from the DM strip translates directly into the same fractional shift in ω, giving $\delta\omega/\omega \sim \phi_{\rm strip}/(\pi/2)$. It is the uniform rescaling of the entire barrier by $e^{-\mathcal{I}}$, not any special sensitivity near $r = 4M_{\rm BH}$, that produces Appendix (B9), with the DM-occupied region adding only this small correction. For $l \geq 3$ both the potential maximum and the turning points lie strictly inside $4M_{\rm BH}$, verified numerically, so the correction is smaller still.

2. Compactness dependence

From Appendix (B9)(A16), $\delta\omega = 1 - e^{-\mathcal{I}/2}$. For fixed halo shape at small compactness $z = M_{\rm halo}/a_0$, the halo integral satisfies $\mathcal{I} \propto z$ (Appendix A 4), so

$$\delta\omega \approx \frac{1}{2}\mathcal{I} \propto z \quad (z \ll 1), \tag{B14}$$

predicting a linear growth of $\delta\omega$ with compactness on a log-log plot, with slope close to unity, matching the initial rise in Fig. 3. As $M_{\rm halo}$ grows, $\mathcal{I}$ grows faster than linear in z since it is convex [Appendix (A17)]. The observable $\delta\omega = 1 - e^{-\mathcal{I}/2}$ is also a strictly growing function in z and is dominantly concave in z (for most of the DM distributions studied in this work), hence the gradual flattening at the right end of Fig. 3. Both the convexity of $\mathcal{I}$ and the monotonic increase of $\delta\omega$ are independent of the specific halo profile, which is why all the curves share the same qualitative shape.

3. Shape-parameter dependence of $\delta\omega$

Since $\delta\omega_{\rm Re} = \delta\omega_{\rm Im} = 1 - e^{-\mathcal{I}/2}$, and $\mathcal{I}$ depends on (α, β, γ) through the mechanisms of Appendix A 3, the shape-parameter trends in Fig. 6 follow directly.

The strong growth of $\delta\omega$ with γ mirrors the growth of $\mathcal{I}$ established in Appendix A 3 a. As γ increases, the dominant radial contribution to $\mathcal{I}$ moves inward from $r \sim a_0$ toward $r \sim 10$–$100M_{\rm BH}$, where the weight $(r - 2M_{\rm BH})^{-1}$ is large. For small $\mathcal{I}$, $\delta\omega \approx \mathcal{I}/2$, and the polynomial behavior seen in the data,

$$\delta\omega \approx \sum_n a_n \gamma^n, \qquad n \geq 0 \tag{B15}$$

follows from a Taylor expansion of $\mathcal{I}(\gamma)$ about $\gamma = 0$. The coefficients a_n encode the sensitivity of the enclosed halo mass to the inner logarithmic slope at each order. At larger γ the growth speeds up because $\mathcal{I}$ increases nonlinearly.

The rise of $\delta\omega$ with β, and its drop with α at larger γ, follow the same mechanisms described for $\delta\Omega_c$ in Appendix A 3, including the same caveats, β's effect is comparable to or weaker than γ's over most of the range shown, but can match or exceed it for small γ or a small gap $\beta - \gamma$, and the α dependence reverses sign below $\gamma \approx 1$.

4. Degeneracy and the iso-$\mathcal{I}$ surface

Equation (B10) shows that $\delta\omega$ depends on $(\alpha, \beta, \gamma, z)$ only through the single number $\mathcal{I}$. Any combination of halo parameters that gives the same $\mathcal{I}$ gives the same $\delta\omega$. In the (γ, z) plane at fixed (α, β), the curves of constant $\delta\omega$ are curves of constant $\mathcal{I}$. Since $\mathcal{I}$ (hence $\delta\omega$) grows strongly with γ, and $\delta\omega$ is an monotonically increasing function of z (numerically observed to be growing concavely with z), a larger γ can offset a smaller z and still give the same total shift, producing the degeneracy curves in Fig. 7.

This degeneracy is exact within the approximation equation (B9). Because $\omega_{\rm DM} = e^{-\mathcal{I}/2}\omega_{\rm Sch}$ for every (l, n) mode, all frequency ratios between modes keep their Schwarzschild values and carry no information about $\mathcal{I}$. Every mode gives the same equation $\delta\omega = 1 - e^{-\mathcal{I}/2}$ independently, so measuring several modes gives redundant determinations of $\mathcal{I}$ but does not pin down which halo parameters $(\alpha, \beta, \gamma, z)$ produce it. The quality factor $Q = \omega_{\rm Re}/|\omega_{\rm Im}|$ is likewise unchanged: $Q_{\rm DM} = Q_{\rm Sch}$ for every mode.

Subleading corrections come from the small portion of the WKB phase integral that extends past $r = 4M_{\rm BH}$, where $m_h(r)$ and $\bar{\rho}(r)$ modify the potential beyond $f(r)$ alone. These corrections are of order $(r_{\rm tp} - 4M_{\rm BH})^{3/2}/\phi_{\rm WKB} \lesssim 10^{-3}$, where $\phi_{\rm WKB}$ is the total WKB phase, and introduce weak mode-dependent contributions to $\delta\omega$ that can differ between modes with different turning-point structures. Such corrections could in principle break the mode degeneracy, but they sit well below current measurement precision.

5. Saturation at large γ

Figures 6 and 7 show $\delta\omega$ growing rapidly with γ but flattening as γ approaches its maximum allowed value β. We now show that this saturation is exact, shared by the eikonal and noneikonal regimes alike, and set by a single computable quantity.

a. Origin of the saturation

From Appendix (B10), both $\delta\Omega_c$ and $\delta\omega_{\rm Re/\,Im}$ equal $1 - e^{-\mathcal{I}/2}$, a monotonically increasing function of $\mathcal{I}$. Since $\mathcal{I}$ is itself increasing in γ, the shifts grow with γ. The physical constraint $\beta > \gamma \geq 0$ sets an upper bound $\gamma < \beta$,

and as $\gamma \to \beta^-$ the profile approaches the pure power-law limit

$$\bar{\rho}(r) \to \bar{\rho}_0 \left(\frac{r}{a_0}\right)^{-\beta} \left(1 - \frac{4M_{\rm BH}}{r}\right) \quad (\gamma \to \beta^-), \tag{B16}$$

where the inner-to-outer transition disappears entirely. This is the most centrally concentrated profile allowed for a given β, so no further inward shift of halo mass is possible. The halo integral then approaches a finite saturation value,

$$\mathcal{I}_{\rm sat}(\beta, M_{\rm halo}) \equiv \mathcal{I}[\bar{\rho} \to \text{Eq. (B16)}, M_{\rm halo}\text{fixed}], \tag{B17}$$

and both the eikonal and noneikonal shifts saturate at the same value,

$$\delta_{\rm sat}(\beta, M_{\rm halo}) = 1 - e^{-\mathcal{I}_{\rm sat}(\beta, M_{\rm halo})/2}. \tag{B18}$$

We write $\mathcal{I}_{\rm sat}$ as a function of $M_{\rm halo}$ rather than of the compactness $z = M_{\rm halo}/a_0$ used elsewhere because, as shown next, a_0 drops out of the limiting profile entirely and $\mathcal{I}_{\rm sat}$ depends on $M_{\rm halo}$ and $M_{\rm BH}$ alone.

b. Normalization of the limiting profile

For the pure power law Appendix (B16) with $\beta > 3$, the total halo mass integral evaluates analytically to

$$M_{\rm halo} = \frac{4\pi \bar{\rho}_0 a_0^\beta (4M_{\rm BH})^{3-\beta}}{(\beta - 3)(\beta - 2)}, \tag{B19}$$

where the factor $[(\beta - 3)(\beta - 2)]^{-1}$ comes from the combined effect of the power-law falloff and the inner cutoff $(1 - 4M_{\rm BH}/r)$. Solving for $\bar{\rho}_0$ and substituting back into the enclosed mass $m_h(r) = \int_{4M_{\rm BH}}^{r} 4\pi r'^2 \bar{\rho}(r') dr'$ shows that every factor of a_0 cancels, leaving

$$\frac{m_h(r)}{M_{\rm halo}} \approx 1 - \left(\frac{4M_{\rm BH}}{r}\right)^{\beta - 3} \quad (r \gg 4M_{\rm BH}), \tag{B20}$$

a function of $r/M_{\rm BH}$ and β alone, with no remaining a_0 dependence. In the $\gamma \to \beta^-$ limit, a_0 no longer marks a transition scale in the density profile, since the profile is a single power law all the way from $4M_{\rm BH}$ to infinity. The scale factor a_0 enters only through normalizing $\bar{\rho}_0$ against $M_{\rm halo}$, and that dependence cancels exactly once the normalization is carried through. Consequently $\mathcal{I}_{\rm sat}$ and $\delta_{\rm sat}$, built entirely from $m_h(r)$ and r, depend on $M_{\rm halo}$ and β only, not on a_0 independently.

c. Saturation value and its dependence on β and $M_{\rm halo}$

The density $\bar{\rho} \propto r^{-\beta}(1 - 4M_{\rm BH}/r)$ peaks at $r_{\rm peak} = 4M_{\rm BH}(1 + \beta)/\beta$, which approaches $4M_{\rm BH}$ monotonically as β grows. A steeper outer profile therefore concentrates the density maximum more tightly near the inner edge of the halo, and the enclosed mass $m_h(r)$ rises more steeply from $r = 4M_{\rm BH}$. Since the integrand of $\mathcal{I}_{\rm sat}$ carries the weight $[r - 2m(r)]^{-1}$, which is largest near $r = 2M_{\rm BH}$, contributions from the inner halo are amplified. A larger β thus raises $\mathcal{I}_{\rm sat}$ and $\delta_{\rm sat}$. For small $M_{\rm halo}/M_{\rm BH}$, $\mathcal{I}_{\rm sat} \propto M_{\rm halo}$ and $\delta_{\rm sat} \approx \mathcal{I}_{\rm sat}/2 \propto M_{\rm halo}$. At larger $M_{\rm halo}$ the nonlinear denominator in Appendix (A16) slows the growth. That a_0 plays no independent role once $\gamma = \beta$ follows directly from the a_0 independence of $m_h(r)/M_{\rm halo}$ in the pure power-law limit established above.

This a_0 independence has a direct consequence for how the saturation appears in figures that hold different quantities fixed. Figure 7 plots $\delta\omega_{\rm Re}$ and $\delta\omega_{\rm Im}$ against γ at fixed $\alpha = 0.5$, $\beta = 3.5$, for three compactnesses $z = 10^{-5}$, $10^{-4.5}$, 10^{-4} obtained by holding a_0 fixed and varying $M_{\rm halo}$. The three curves remain separated by roughly an order of magnitude across the full range, including as $\gamma \to \beta^-$: they do not converge at the right edge of the plot. This is expected, since $\delta_{\rm sat}$ depends directly on $M_{\rm halo}$, which differs between the three curves. The successive terminal values increase faster than the linear-in-$M_{\rm halo}$ scaling that holds only once $\mathcal{I}_{\rm sat}$ is small, consistent with the convex growth of $\mathcal{I}$ with compactness established in Appendix A 4.

Figure 4, by contrast, obtains its different compactnesses by holding $M_{\rm halo}$ fixed and varying a_0 instead. Because $\mathcal{I}_{\rm sat}$ does not depend on a_0, the curves shown there for different a_0 at the same $M_{\rm halo}$ converge to a common value as $\gamma \to \beta^-$, in contrast with Fig. 7. The two figures are therefore not in tension: each varies a different one of the two independent quantities entering $z = M_{\rm halo}/a_0$, and only $M_{\rm halo}$ survives in the saturated limit.

d. Observational implication

A finite saturation means that for a given $(\beta, M_{\rm halo})$ there is a maximum frequency redshift reachable by varying γ. A measured $\delta\omega$ above $\delta_{\rm sat}(\beta, M_{\rm halo})$ would be inconsistent with the (α, β, γ) family at that halo mass, giving a direct constraint on the halo parameters. A measured shift below $\delta_{\rm sat}$ is consistent with a range of γ values, feeding into the degeneracy discussed in Appendixes A 4 and B 4. Because $\delta_{\rm sat}$ depends on $M_{\rm halo}$ rather than on a_0, as Figs. 4 and 7 together show, this saturation bound constrains γ once $(\beta, M_{\rm halo})$ are otherwise fixed or independently known, regardless of a_0.

[1] B. P. Abbott *et al.* (LIGO Scientific and Virgo Collaborations), Observation of gravitational waves from a binary black hole merger, Phys. Rev. Lett. **116**, 061102 (2016).

[2] E. Berti *et al.*, Black hole spectroscopy: From theory to experiment, Classical Quantum Gravity **43**, 123001 (2026).

[3] B. P. Abbott *et al.* (LIGO Scientific and Virgo Collaborations), GWTC-1: A gravitational-wave transient catalog of compact binary mergers observed by LIGO and Virgo during the first and second observing runs, Phys. Rev. X **9**, 031040 (2019).

[4] R. Abbott *et al.* (LIGO Scientific and Virgo Collaborations), GWTC-2: Compact binary coalescences observed by LIGO and Virgo during the first half of the third observing run, Phys. Rev. X **11**, 021053 (2021).

[5] R. Abbott *et al.* (KAGRA, Virgo, and LIGO Scientific Collaborations), GWTC-3: Compact binary coalescences observed by LIGO and Virgo during the second part of the third observing run, Phys. Rev. X **13**, 041039 (2023).

[6] A. G. Abac *et al.* (LIGO Scientific and KAGRA Collaborations), GWTC-4.0: Updating the gravitational-wave transient catalog with observations from the first part of the fourth LIGO-Virgo-KAGRA observing run, Astrophys. J. Lett. **1004** (2026) L22.

[7] LIGO Scientific, Virgo, and KAGRA Collaborations, GWTC-5.0: Constraints on the cosmic expansion rate and modified gravitational-wave propagation, arXiv:2605.27227.

[8] A. G. Abac *et al.* (LIGO Scientific, Virgo, and KAGRA Collaborations), GWTC-5.0: Methods for identifying and characterizing gravitational-wave transients,

[9] C. V. Vishveshwara, Scattering of gravitational radiation by a Schwarzschild black-hole, Nature (London) **227**, 936 (1970).

[10] E. Berti, V. Cardoso, and A. O. Starinets, Quasinormal modes of black holes and black branes, Classical Quantum Gravity **26**, 163001 (2009).

[11] C. V. Vishveshwara, Stability of the Schwarzschild metric, Phys. Rev. D **1**, 2870 (1970).

[12] W. H. Press, Long wave trains of gravitational waves from a vibrating black hole, Astrophys. J. Lett. **170**, L105 (1971).

[13] S. Chandrasekhar, *The Mathematical Theory of Black Holes* (Clarendon Press, Oxford, 1983).

[14] K. D. Kokkotas and B. G. Schmidt, Quasinormal modes of stars and black holes, Living Rev. Relativity **2**, 2 (1999).

[15] R. A. Konoplya and A. Zhidenko, Quasinormal modes of black holes: From astrophysics to string theory, Rev. Mod. Phys. **83**, 793 (2011).

[16] P. Amaro-Seoane *et al.* (LISA Collaboration), Laser interferometer space antenna, arXiv:1702.00786.

[17] V. Baibhav, E. Berti, and V. Cardoso, LISA parameter estimation and source localization with higher harmonics of the ringdown, Phys. Rev. D **101**, 084053 (2020).

[18] L. Piro *et al.*, Chasing super-massive black hole merging events with *Athena* and LISA, Mon. Not. R. Astron. Soc. **521**, 2577 (2023).

[19] P. A. Seoane *et al.* (LISA Collaboration), Astrophysics with the laser interferometer space antenna, Living Rev. Relativity **26**, 2 (2023).

[20] S. Deng, S. Babak, and S. Marsat, Fast detection and reconstruction of merging massive black hole binary signals, Phys. Rev. D **112**, 043010 (2025).

[21] E. Berti *et al.*, Testing general relativity with present and future astrophysical observations, Classical Quantum Gravity **32**, 243001 (2015).

[22] V. Cardoso and P. Pani, Testing the nature of dark compact objects: A status report, Living Rev. Relativity **22**, 4 (2019).

[23] E. Barausse, V. Cardoso, and P. Pani, Can environmental effects spoil precision gravitational-wave astrophysics?, Phys. Rev. D **89**, 104059 (2014).

[24] A. M. Ghez *et al.*, Measuring distance and properties of the milky way's central supermassive black hole with stellar orbits, Astrophys. J. **689**, 1044 (2008).

[25] S. Gillessen, F. Eisenhauer, S. Trippe, T. Alexander, R. Genzel, F. Martins, and T. Ott, Monitoring stellar orbits around the massive black hole in the galactic center, Astrophys. J. **692**, 1075 (2009).

[26] M. Miyoshi, J. Moran, J. Herrnstein, L. Greenhill, N. Nakai, P. Diamond, and M. Inoue, Evidence for a black hole from high rotation velocities in a sub-parsec region of NGC4258, Nature (London) **373**, 127 (1995).

[27] J. Kormendy and L. C. Ho, Coevolution (Or Not) of supermassive black holes and host galaxies, Annu. Rev. Astron. Astrophys. **51**, 511 (2013).

[28] L. Ferrarese and D. Merritt, A fundamental relation between supermassive black holes and their host galaxies, Astrophys. J. Lett. **539**, L9 (2000).

[29] K. Gebhardt *et al.*, A relationship between nuclear black hole mass and galaxy velocity dispersion, Astrophys. J. Lett. **539**, L13 (2000).

[30] J. F. Navarro, C. S. Frenk, and S. D. M. White, The structure of cold dark matter halos, Astrophys. J. **462**, 563 (1996).

[31] J. F. Navarro, C. S. Frenk, and S. D. M. White, A universal density profile from hierarchical clustering, Astrophys. J. **490**, 493 (1997).

[32] P. Salucci, The distribution of dark matter in galaxies, Astron. Astrophys. Rev. **27**, 2 (2019).

[33] A. Chowdhury, G. Sen, S. Chakrabarti, and S. Das, Effect of generic dark matter halos on the transonic accretion onto galactic black holes, Phys. Rev. D **112**, 064041 (2025).

[34] A. Chowdhury, G. Sen, S. Chakrabarti, and S. Das, Dark matter halos and transonic accretion flow, J. Phys. Conf. Ser. **3177**, 012038 (2026).

[35] C. F. B. Macedo, J. a. L. Rosa, and D. Rubiera-Garcia, Optical appearance of black holes surrounded by a dark matter halo, J. Cosmol. Astropart. Phys. 07 (2024) 046.

[36] D. S. Fonseca, C. F. B. Macedo, M. Malato Corrêa, and D. Rubiera-Garcia, Matter environments around black holes: Geodesics, light rings, and ultracompact configurations, Phys. Rev. D **113**, 124039 (2026).

[37] A. L. Miller, Gravitational wave probes of particle dark matter: A review, Int. J. Mod. Phys. D **35**, 2530005 (2026).

[38] F. Dosopoulou and J. Silk, Multimessenger detection of black hole binaries in dark matter spikes, Phys. Rev. Lett. **135**, 081401 (2025).

[39] G. Bertone, Dark matter, black holes, and gravitational waves, Nucl. Phys. **B1003**, 116487 (2024).

[40] P. Gondolo and J. Silk, Dark matter annihilation at the galactic center, Phys. Rev. Lett. **83**, 1719 (1999).
[41] L. Sadeghian, F. Ferrer, and C. M. Will, Dark matter distributions around massive black holes: A general relativistic analysis, Phys. Rev. D **88**, 063522 (2013).
[42] O. Y. Gnedin and J. R. Primack, Dark matter profile in the galactic center, Phys. Rev. Lett. **93**, 061302 (2004).
[43] D. Merritt, M. Milosavljevic, L. Verde, and R. Jimenez, Dark matter spikes and annihilation radiation from the galactic center, Phys. Rev. Lett. **88**, 191301 (2002).
[44] D. Merritt, Evolution of the dark matter distribution at the galactic center, Phys. Rev. Lett. **92**, 201304 (2004).
[45] P. Ullio, H. Zhao, and M. Kamionkowski, A dark matter spike at the galactic center?, Phys. Rev. D **64**, 043504 (2001).
[46] G. Bertone *et al.*, Gravitational wave probes of dark matter: Challenges and opportunities, SciPost Phys. Core **3**, 007 (2020).
[47] K. Eda, Y. Itoh, S. Kuroyanagi, and J. Silk, New probe of dark-matter properties: Gravitational waves from an intermediate-mass black hole embedded in a dark-matter minispike, Phys. Rev. Lett. **110**, 221101 (2013).
[48] R. A. Konoplya, Black holes in galactic centers: Quasinormal ringing, grey-body factors and Unruh temperature, Phys. Lett. B **823**, 136734 (2021).
[49] R. A. Konoplya and A. Zhidenko, Solutions of the Einstein equations for a black hole surrounded by a galactic halo, Astrophys. J. **933**, 166 (2022).
[50] V. Cardoso, K. Destounis, F. Duque, R. Panosso Macedo, and A. Maselli, Gravitational waves from extreme-mass-ratio systems in astrophysical environments, Phys. Rev. Lett. **129**, 241103 (2022).
[51] E. Figueiredo, A. Maselli, and V. Cardoso, Black holes surrounded by generic dark matter profiles: Appearance and gravitational-wave emission, Phys. Rev. D **107**, 104033 (2023).
[52] N. Speeney, E. Berti, V. Cardoso, and A. Maselli, Black holes surrounded by generic matter distributions: Polar perturbations and energy flux, Phys. Rev. D **109**, 084068 (2024).
[53] L. Pezzella, K. Destounis, A. Maselli, and V. Cardoso, Quasinormal modes of black holes embedded in halos of matter, Phys. Rev. D **111**, 064026 (2025).
[54] A. Einstein, On a stationary system with spherical symmetry consisting of many gravitating masses, Ann. Math. **40**, 922 (1939).
[55] A. Geralico, F. Pompi, and R. Ruffini, On Einstein clusters, Int. J. Mod. Phys. Conf. Ser. **12**, 146 (2012).
[56] S. Chakraborty, G. Compère, and L. Machet, Tidal Love numbers and quasinormal modes of the Schwarzschild-Hernquist black hole, Phys. Rev. D **112**, 024015 (2025).
[57] S. Iyer and C. M. Will, Black hole normal modes: A WKB Approach. 1. Foundations and application of a higher order WKB analysis of potential barrier scattering, Phys. Rev. D **35**, 3621 (1987).
[58] B. F. Schutz and C. M. Will, Black hole normal modes: A semianalytic approach, Astrophys. J. Lett. **291**, L33 (1985).
[59] R. A. Konoplya, Quasinormal behavior of the d-dimensional Schwarzschild black hole and higher order WKB approach, Phys. Rev. D **68**, 024018 (2003).
[60] C. Gundlach, R. H. Price, and J. Pullin, Late time behavior of stellar collapse and explosions: 1. Linearized perturbations, Phys. Rev. D **49**, 883 (1994).
[61] V. Cardoso, A. S. Miranda, E. Berti, H. Witek, and V. T. Zanchin, Geodesic stability, Lyapunov exponents and quasinormal modes, Phys. Rev. D **79**, 064016 (2009).
[62] T. Binnington and E. Poisson, Relativistic theory of tidal Love numbers, Phys. Rev. D **80**, 084018 (2009).
[63] T. Damour and A. Nagar, Relativistic tidal properties of neutron stars, Phys. Rev. D **80**, 084035 (2009).
[64] B. Kol and M. Smolkin, Black hole stereotyping: Induced gravito-static polarization, J. High Energy Phys. 02 (2012) 010.
[65] S. Chakrabarti, T. Delsate, and J. Steinhoff, New perspectives on neutron star and black hole spectroscopy and dynamic tides, arXiv:1304.2228.
[66] N. Gürlebeck, No-hair theorem for black holes in astrophysical environments, Phys. Rev. Lett. **114**, 151102 (2015).
[67] H. S. Chia, Tidal deformationand dissipation of rotating black holes, Phys. Rev. D **104**, 024013 (2021).
[68] R. P. Bhatt, S. Chakraborty, and S. Bose, Addressing issues in defining the Love numbers for black holes, Phys. Rev. D **108**, 084013 (2023).
[69] A. Le Tiec, M. Casals, and E. Franzin, Tidal Love numbers of Kerr black holes, Phys. Rev. D **103**, 084021 (2021).
[70] P. Charalambous, S. Dubovsky, and M. M. Ivanov, On the vanishing of Love numbers for Kerr black holes, J. High Energy Phys. 05 (2021) 038.
[71] S. Chakraborty, P. Heidmann, and P. Pani, Fermionic response of black holes in general relativity, Phys. Rev. D **113**, L061503 (2026).
[72] S. Chakraborty and P. Pani, Tidal response of compact objects, arXiv:2604.08679.
[73] M. J. Rodríguez, L. Santoni, and A. R. Solomon, Love numbers of black holes and compact objects, arXiv:2604.08653.
[74] A. Chowdhury, C. Singha, K. Bamba, and S. Chakraborty, Tidal deformation of an accreting compact object, arXiv:2607.24938.
[75] V. Cardoso, L. Gualtieri, and C. J. Moore, Gravitational waves and higher dimensions: Love numbers and Kaluza-Klein excitations, Phys. Rev. D **100**, 124037 (2019).
[76] L. Hui, A. Joyce, R. Penco, L. Santoni, and A. R. Solomon, Static response and Love numbers of Schwarzschild black holes, J. Cosmol. Astropart. Phys. 04 (2021) 052.
[77] V. De Luca, A. Garoffolo, J. Khoury, and M. Trodden, Tidal Love numbers and Green's functions in black hole spacetimes, Phys. Rev. D **110**, 064081 (2024).
[78] R. P. Bhatt and C. Singha, Scalar tidal response of a rotating BTZ black hole, J. High Energy Phys. 11 (2024) 154.
[79] K. Chakravarti, S. Chakraborty, S. Bose, and S. SenGupta, Tidal Love numbers of black holes and neutron stars in the presence of higher dimensions: Implications of GW170817, Phys. Rev. D **99**, 024036 (2019).

[80] M. J. Rodriguez, L. Santoni, A. R. Solomon, and L. F. Temoche, Love numbers for rotating black holes in higher dimensions, Phys. Rev. D **108**, 084011 (2023).
[81] V. Cardoso, M. Kimura, A. Maselli, and L. Senatore, Black holes in an effective field theory extension of general relativity, Phys. Rev. Lett. **121**, 251105 (2018).
[82] V. Cardoso, E. Franzin, A. Maselli, P. Pani, and G. Raposo, Testing strong-field gravity with tidal Love numbers, Phys. Rev. D **95**, 084014 (2017).
[83] V. De Luca, J. Khoury, and S. S. C. Wong, Implications of the weak gravity conjecture for tidal Love numbers of black holes, Phys. Rev. D **108**, 044066 (2023).
[84] C. Singha and S. Chakraborty, Tidal deformation of black holes in Lovelock gravity, Phys. Rev. D **113**, 024005 (2026).
[85] R. Emparan, A. Fernandez-Pique, and R. Luna, Geometric polarization of plasmas and Love numbers of AdS black branes, J. High Energy Phys. 09 (2017) 150.
[86] S. Nair, S. Chakraborty, and S. Sarkar, Asymptotically de Sitter black holes have nonzero tidal Love numbers, Phys. Rev. D **109**, 064025 (2024).
[87] E. Franzin, A. M. Frassino, and J. V. Rocha, Tidal Love numbers of static black holes in anti-de Sitter, J. High Energy Phys. 12 (2025) 224.
[88] M. Silvestrini, E. Maggio, S. Chakraborty, and P. Pani, Tidal deformations of compact objects from the membrane paradigm, Phys. Rev. D **112**, 124021 (2025).
[89] S. Chakraborty, E. Maggio, M. Silvestrini, and P. Pani, Dynamical tidal Love numbers of Kerr-like compact objects, Phys. Rev. D **110**, 084042 (2024).
[90] S. Nair, S. Chakraborty, and S. Sarkar, Dynamical Love numbers for area quantized black holes, Phys. Rev. D **107**, 124041 (2023).
[91] P. Pani, L. Gualtieri, A. Maselli, and V. Ferrari, Tidal deformations of a spinning compact object, Phys. Rev. D **92**, 024010 (2015).
[92] K. Chakravarti and C. Singha, Tidal Love numbers and quasi-normal modes of the ECO in a dark matter halo, arXiv:2509.03556.
[93] V. Cardoso and F. Duque, Environmental effects in gravitational-wave physics: Tidal deformability of black holes immersed in matter, Phys. Rev. D **101**, 064028 (2020).
[94] V. Cardoso, K. Destounis, F. Duque, R. P. Macedo, and A. Maselli, Black holes in galaxies: Environmental impact on gravitational-wave generation and propagation, Phys. Rev. D **105**, L061501 (2022).
[95] S. D'Onofrio, S. Datta, and A. Maselli, Axial tidal Love numbers of black holes in matter environments, arXiv:2605.02633.
[96] Y.-Q. Zhao and P. Pani, Quasinormal modes and tidal responses of black holes in generic anisotropic matter environments, arXiv:2606.11380.
[97] E. Cannizzaro, V. De Luca, and P. Pani, Tidal deformability of black holes surrounded by thin accretion disks, Phys. Rev. D **110**, 123004 (2024).
[98] P. Amaro-Seoane *et al.*, Low-frequency gravitational-wave science with eLISA/NGO, Classical Quantum Gravity **29**, 124016 (2012).
[99] A. Coogan, G. Bertone, D. Gaggero, B. J. Kavanagh, and D. A. Nichols, Measuring the dark matter environments of black hole binaries with gravitational waves, Phys. Rev. D **105**, 043009 (2022).
[100] F. Duque, C. F. B. Macedo, R. Vicente, and V. Cardoso, Extreme-mass-ratio inspirals in ultralight dark matter, Phys. Rev. Lett. **133**, 121404 (2024).
[101] Y. Zhao, N. Dai, and Y. Gong, Distinguishing dark matter haloes with extreme mass ratio inspirals, Mon. Not. R. Astron. Soc. **543**, 2326 (2025).
[102] J. E. Taylor and J. Silk, The clumpiness of cold dark matter: Implications for the annihilation signal, Mon. Not. R. Astron. Soc. **339**, 505 (2003).
[103] A. Dekel, G. Ishai, A. A. Dutton, and A. V. Maccio, Dark-matter halo profiles of a general cusp/core with analytic velocity and potential, Mon. Not. R. Astron. Soc. **468**, 1005 (2017).
[104] H. Zhao, Analytical models for galactic nuclei, Mon. Not. R. Astron. Soc. **278**, 488 (1996).
[105] J. Einasto, The Andromeda galaxy M31. I. A preliminary model, Astrofiz. **5**, 137 (1969).
[106] R. Acharyya, P. Banerjee, and S. Kar, Modelling Einstein cluster using einasto profile, J. Cosmol. Astropart. Phys. 04 (2024) 070.
[107] A. W. Graham, D. Merritt, B. Moore, J. Diemand, and B. Terzic, Empirical models for dark matter halos. I. Nonparametric construction of density profiles and comparison with parametric models, Astron. J. **132**, 2685 (2006).
[108] F. Prada, A. A. Klypin, E. Simonneau, J. Betancort-Rijo, S. Patiri, S. Gottlober, and M. A. Sanchez-Conde, How far do they go? The outer structure of dark matter halos, Astrophys. J. **645**, 1001 (2006).
[109] P. V. P. Cunha and C. A. R. Herdeiro, Stationary black holes and light rings, Phys. Rev. Lett. **124**, 181101 (2020).
[110] R. Ghosh, S. Sk, and S. Sarkar, Hairy black holes: Nonexistence of short hairs and a bound on the light ring size, Phys. Rev. D **108**, L041501 (2023).
[111] T. Regge and J. A. Wheeler, Stability of a Schwarzschild singularity, Phys. Rev. **108**, 1063 (1957).
[112] E. W. Leaver, An analytic representation for the quasi normal modes of Kerr black holes, Proc. R. Soc. A **402**, 285 (1985).
[113] Y. Zhao, B. Sun, K. Lin, and Z. Cao, Axial gravtational ringing of a spherically symmetric black hole surrounded by dark matter spike, Phys. Rev. D **108**, 024070 (2023).
[114] A. G. Abac *et al.* (LIGO Scientific, Virgo, and KAGRA Collaborations), Black hole spectroscopy and tests of general relativity with GW250114, Phys. Rev. Lett. **136**, 041403 (2026).
[115] A. G. Abac *et al.* (LIGO Scientific, Virgo, and KAGRA Collaborations), GW250114: Testing Hawking's area law and the Kerr nature of black holes, Phys. Rev. Lett. **135**, 111403 (2025).
[116] R. F. Rosato and P. Pani, Universality of late-time ringdown tails, Phys. Rev. D **112**, 024080 (2025).
[117] N. Andersson, Evolving test fields in a black hole geometry, Phys. Rev. D **55**, 468 (1997).
[118] T. F. M. Spieksma, V. Cardoso, G. Carullo, M. Della Rocca, and F. Duque, Black hole spectroscopy in

environments: Detectability prospects, Phys. Rev. Lett. **134**, 081402 (2025).

[119] E. Berti, V. Cardoso, J. A. Gonzalez, and U. Sperhake, Mining information from binary black hole mergers: A comparison of estimation methods for complex exponentials in noise, Phys. Rev. D **75**, 124017 (2007).

[120] R. Ghosh, R. P. Bhatt, S. Chakraborty, and S. Bose, Universal ladder structure across scales: From quantum to black hole physics, arXiv:2604.06249.

[121] W. E. Boyce, R. C. DiPrima, and D. B. Meade, *Elementary Differential Equations and Boundary Value Problems*, 12 ed. (Wiley, Hoboken, NJ, 2021).

[122] R. Ghosh, N. Speeney, A. Chowdhury, C. Singha, M. A. S. Pinto and E. Berti, From density to mass: A new parametrized framework for dark matter environment around black holes, arXiv:2609.35771.

[123] T. Miyachi, R. Namba, H. Omiya, and N. Oshita, Path to an exact WKB analysis of black hole quasinormal modes, Phys. Rev. D **111**, 124045 (2025).